

1 **Slope stability models for rainfall-induced lahars during long-lasting eruptions**

2 List of authors: Valérie Baumann⁽¹⁾, Costanza Bonadonna⁽¹⁾, Sabatino Cuomo⁽²⁾, Mariagiovanna
3 MoscarIELlo⁽²⁾, Irene Manzella⁽³⁾

4

5 ⁽¹⁾Department of Earth Sciences, University of Geneva, Rue des Maraîchers 13, 1205 Geneva,
6 Switzerland

7 ⁽²⁾Laboratory of Geotechnics, University of Salerno

8 Via Giovanni Paolo II 132, 84081 Fisciano (Salerno), Italy

9 ⁽³⁾School of Geography, Earth, and Environmental Sciences, Plymouth University, Drake Circus,
10 Plymouth, UK

11

12 **Abstract**

13 In this study we analyse the spatial distribution of potential lahar sources during long-lasting eruptions
14 using two slope stability models (SHALSTAB and TRIGRS). The analysis is based on observed deposit
15 grain-size and thickness, rainfall data and slope angle of the lahar events, in the area surrounding the
16 Cordón Caulle volcano, Chile, that occurred during the 2011 eruption. The main phase of the eruption
17 (4-7 June) was characterized by eruptive plumes from 7 to 11 km high which dispersed most of the
18 tephra eastward toward Argentina, with a total estimated volume of about 1 km³. Tephra fall blanketed
19 the region from ESE to ENE of the volcano with the thickness of the tephra layers between
20 approximately 1 m (15 km from vent) and 0.06 m (240 km from the vent). On 10 June 2011, a major
21 lahar occurred close to the Argentina-Chile border that reached the National road 231 (28 km from the
22 vent). Three field campaigns were undertaken to collect samples and data from tephra deposits and
23 triggering mechanisms in the lahar source area. Model input parameters were obtained from
24 geotechnical test and field measurements. Several metrics are used for model evaluation and best fit to
25 the data are obtained for simulations considering non-cohesive ash layers for SHALSTAB and a
26 cohesion of 0.5 kPa for TRIGRS. Both models are sensitive to the physical properties of the tephra
27 deposit and the hydraulic and material strength properties of the study area. They both also show good
28 agreement with field data but provide different information: TRIGRS provides an estimate of the timing
29 (based on a storm event) and location of a potentially unstable area, while SHALSTAB simulations
30 result in landslide susceptibility classes based on critical rainfall value. These outcomes provide
31 fundamental insights into lahar triggering during long-lasting volcanic eruptions and are crucial to the
32 compilation of lahar hazard maps and emergency management plans in the South Andes volcanic region.

33

34 **Keywords:** lahar, initiation mechanism, SHALSTAB, TRIGRS, Cordón Caulle volcano

35

36

37 **1. Introduction**

38 Lahars are widespread phenomena in volcanic areas that can severely affect people and infrastructure
39 (Pierson et al., 1990; Pierson et al., 1992; Janda et al., 1996; Scott et al., 2005; Scott et al., 1996; Lavigne
40 et al., 2000a). Historical cases of deadly lahars such as Mt Pinatubo, Philippines (Pierson et al., 1992),
41 Nevado del Ruiz, Colombia (Pierson et al., 1990), Casita Volcano, Nicaragua (Scott et al., 2005), and
42 Panabaj, Guatemala (Charbonnier et al., 2018), demonstrate that they represent one of the most
43 significant hazards to people living in volcanic areas. The lahars generated years after the 1991 eruption
44 of Mt. Pinatubo (Janda et al., 1996) constitute the most voluminous and devastatingly widespread, as
45 well as one of the most long-lasting lahar episodes, ever recorded.

46 “Lahar” is an Indonesian term for a mixture of rock debris and water that flows downslope, beyond
47 normal streamflows (Smith, 1986; Smith and Lowe, 1991; Vallance, 2000). The term is genetic rather
48 than descriptive, encompassing a wide spectrum of sediment to water ratios and flow rheologies
49 (Manville et al., 2009). Lahars can be caused directly by eruptive activity or during post-eruptive or
50 quiescent periods. They are mainly generated by the remobilization of tephra-fallout and Pyroclastic
51 Density Current (PDC) deposits, but may also form from a previously emplaced debris avalanche
52 produced by the gravitational collapse and disintegration of the volcano edifice (Pierson et al. 2014).
53 After explosive volcanic eruptions, PDC deposits fill valleys and tephra-fallout deposits may blanket
54 the volcano flanks and, when the intensity of the explosive eruption is high enough, topographic reliefs
55 even hundreds of kilometres from the source.

56 Tephra-fallout deposits are unconsolidated, loose and highly erodible during rainstorms (Pierson and
57 Major, 2014). It is well documented that explosive eruptions can drastically alter drainage basin
58 hydrology and erosion processes (Pierson and Major, 2014). Many researchers have also reported poor
59 infiltration capacity of freshly deposited tephra following volcanic explosions, producing surface flow
60 over barren hillslopes (Collins and Dunne 1986; Leavesly et al. 1989; Major et al., 2000; Pierson et al.,
61 2013; Major and Yamakoshi, 2005; Yamakoshi and Suwa, 2000; Yamamoto 1984).

62 Most of the available lahar-hazard assessments are based on the analysis of lahar spreading areas
63 (Manville et al., 2013). Models routinely used include the empirical model LAHARZ (Iverson et al.,
64 1998) and the more complex Titan 2D model (Sheridan et al., 2005). Numerical models based on depth-
65 averaged continuum flow equations are also used for lahar hazard evaluation, such as FLO-2D (O’Brian
66 et al., 1993) at Nevado del Huila, Colombia (Worni et al., 2012), Popocatepetl, Mexico (Caballero and
67 Capra, 2014; Caballero et al. 2016) and Panabaj, Guatemala (Charbonnier et al., 2018). Haddad et al.
68 (2010) also used a Smoothed Particle Hydrodynamics (SPH) depth-integrated model for simulating
69 lahar spreading on Popocatepetl volcano. Besides, analysis of rainfall intensity and duration thresholds
70 for lahar triggering mechanisms have been performed at many volcanoes, e.g. Mount Pinatubo (Van
71 Westen and Daag, 2005), Indonesia (Lavigne et al., 2000a; Lavigne et al., 2000b; Lavigne and Suwa,
72 2004), Mexico (Capra et al., 2010), and Montserrat (Barclay et al., 2007).

73 Predicting the initiation area is crucial to assessments of rainfall triggered lahar volumes and potential
74 runoff (Iverson, 1997). Rain-triggered lahars are associated with two main mechanisms: sheet and rill

75 erosion by Hortonian overland flow due to deposit saturation (Collins and Dunne, 1986; Cuomo et al.,
76 2015) and rain infiltration that can induce shallow landslides (Iverson and Lahusen, 1989; Manville et
77 al., 2000; Crosta and Dal Negro, 2003; Zanchetta et al., 2004; Volentik et al., 2009; Cascini et al., 2010).
78 Spatially distributed simulations of unsaturated tephra-fallout deposit failure is usually performed using
79 hydrological models coupled with infinite slope stability. Such models have been developed following
80 the catastrophic landslides and flow events in Sarno, 1998 and similar areas in the Campania region in
81 South Italy (Cascini et al., 2010; Frattini et al., 2004; Crosta and Dal Negro, 2003; Cuomo and Iervolino,
82 2016; Cuomo and Della Sala, 2016; Cascini et al., 2011; Sorbino et al. 2007, 2010). In addition, Volentik
83 et al. (2009) proposed an infinite slope failure criterion (Iverson, 2000) for the evaluation of lahar source
84 areas at Mt Natib volcano, Indonesia, and Mead et al. (2016) presented a study on rain triggered lahar
85 susceptibility using shallow landslide and erosion models.

86 Nevertheless, even if the main parameters for lahar triggering have been identified, how failure
87 mechanisms vary during long lasting eruptions, i.e. those lasting from a few days to several months or
88 years, remains an open question. In fact, the effect of the variation of parameters, such as the thickness,
89 grainsize and composition of tephra layers and of the rainfall intensity and frequency over long periods
90 of time, on slope stability is difficult to model accurately. For this reason, analysis of well-documented
91 case studies is crucial for understanding such complex process, and for empirical assessment of the
92 above-mentioned thresholds.

93 In this paper, we present a detailed study of events that occurred during the 1 year eruption of Cordón
94 Caulle (Chile) in 2011-2012, and we have analyse factors that may influence the triggering of rainfall
95 induced lahars in such a variable and complex system. We take into account several different parameters,
96 including the extension of the source areas, amount of water, slope gradient, and the physical
97 characteristics and thickness of the source deposit. Two watersheds with recorded lahar events, located
98 50 km from the Cordón Caulle vent area, have been studied in the field and used for back analysis using
99 two shallow stability models, SHALSTAB and TRIGRS. In particular, variations in the number of
100 layers, layer thickness and composition, and rainfall intensity and duration were considered in the
101 numerical simulations.

102 This combination of detailed field and laboratory studies, and back analysis of well constrained events
103 with two distinct numerical models has thus contributed in improving our understanding of the triggering
104 processes of these extremely dangerous phenomena and has helped us improve the related hazard
105 assessment in the variable and complex environment provided by long-lasting volcanic eruptions.

106

107 **2. The study area**

108

109 **2.1 The 2011 eruption of Cordón Caulle**

110 The case study includes several lahar-prone basins near the Argentina-Chile border and in Villa La
111 Angostura, Argentina. The area is in the Southern Andes, east of the Cordón Caulle volcano, along the

112 main ash dispersal axis and road N. 231 and between 28 and 50 km from the vent area (Fig. 1). Here,
113 the southern Andes have an average elevation of about 1500 m. The landscape is characterized by
114 glacially sculpted steep slopes, glacial and tectonic lakes, and flat valley floors of fluvial and glacio-
115 fluvial outwash. During the Pleistocene a lobe of the Cordilleran ice sheet occupied the study area. U-
116 shaped valleys, many cirques, moraine and erosive glacial features (roches moutonnées) are evidence
117 of the Pleistocene glaciation. Most of the post-glaciation erosive surfaces are covered by Holocene
118 tephra sequences with ages ranging from 10 to 1.1 ka (Singer et al., 2008; Naranjo et al., 2017). Naranjo
119 et al. (2017) described a Holocene tephra succession, near Villa La Angostura, composed mainly of
120 lapilli pumice, lapilli scoria, ash and paleo-soils with a total thickness of 4.6 m. The old basement
121 consists of Cretaceous volcanic rocks (diorites, granodiorites) and outcrops on the summit of Cerro
122 Bayo. The whole area is densely vegetated, covered by the Valdivian rain forest composed mainly of
123 trees from the *Nothofagus* genus (lengas and ñires). The climate is cold with an average temperature of
124 10° C and annual precipitation varying between 800 and 2500 mm.

125
126 On 4 June 2011, the Puyehue-Cordón Caulle volcanic complex (Central Andes, Fig.1) erupted from
127 multiple vents along a NW-SE fracture in the Cordón Caulle system (CC) system (Castro et al., 2013;
128 Pistolesi et al., 2015). The main phase (4-7 June), characterized by plumes heights of 7 to 11 km,
129 dispersed about 1 km³ of tephra towards Argentina and deposited between 1 m (15 km from vent) and 6
130 cm (240 km from the vent) of tephra on the ground (Fig. 1). The eruption continued for several months
131 with lava effusion and low intensity ash emissions. A red alert was lowered to orange in March 2012,
132 10 months after the main phase (Elissondo et al., 2016).

133 The eruptive sequence was divided into 3 main tephra units: I, II, and III (Pistolesi et al., 2015). At
134 outcrops 25 to 50 km from the vent, the sequences appear as two, stratified, fine lapilli bearing
135 depositional units (I and II), covered by a third unit composed of multiple fine ash layers interbedded
136 with thin coarse ash to fine lapilli beds (III) (Fig. 2). Unit I was emplaced during the first 24-30 hours
137 of the eruption (4 and 5 June) and unit II was emplaced during 5-7 June. Finally, unit III was mostly
138 emplaced from 7 until 15 June, although millimetres of fine tephra also sedimented during later low
139 level activity.

140 Tephra fallout produced several impacts on population, animals and vegetation (Elissondo et al., 2016).
141 After the main explosive phase (4-7 June) a large volume of tephra mantled the steep hillslopes of the
142 U-shaped valley in the surrounding area of the volcano (Fig. 1a).

143

144 **2.2 Lahars, floods and snow avalanche events following tephra-fallout deposition (2011-2012)**

145 In this section we describe lahar, flood and snow avalanche events, including both data obtained from
146 field campaigns, during and after the eruption, and reports, photos and oral communications made
147 during the volcanic eruption by the Villa La Angostura Civil Defence and Mountain rescue group.

148 During the wet season, loose and unconsolidated tephra was transported through steep channels, and

149 lahars reached the valley bottom. Many lahars and related flood events were observed between the
150 Argentina-Chile border and Villa la Angostura (48 km from the vent). The tephra-fallout thickness, as
151 measured on 10 June was between 30 and 40 cm near the Argentina-Chile border and 12 and 15 cm at
152 Villa La Angostura (Pistolesi et al., 2015). The eruption and subsequent tephra-fallout coincided with
153 the beginning of winter. In June, precipitation was falling as rain at 800 m, and as snow at 1,500 m.
154 Total precipitation accumulated between 7 and 10 June was 116 cm. Figure 3a and b illustrate the daily
155 rainfall and the timing of lahar and floods events near both the Chile-Argentina Border (Rincon rain
156 gauge) and Villa La Angostura between June 2011 and June 2012.

157 The most destructive lahar event occurred on 10 June 2011, during the first week after the eruption
158 onset, flowing down a channel on Cerro Las Tres Hermanas (28 km from the vent area, Fig. 1b). The
159 volcanic material coming down the creek blocked the culvert below the road and flowed on to road N.
160 231, eroding and destroying the asphalt (Red triangle “L2” on Fig. 1b and Fig. 4a). The flow cross
161 section upstream of the road was estimated at 80 m². One hundred meters upstream of road N. 231, we
162 identified 3 main lobes of lahar deposits crossing the forest. A stratigraphic section, of thickness 1.39
163 m, from an exposure in the main creek revealed 5 beds with 2 different lithofacies. Figure 5a shows the
164 stratigraphy of the lahar deposit with 2 different lithofacies, types A and B. Type A is an inversely
165 graded, massive, pumice rich, coarse sand to fine gravel, supported in a fine sand silty matrix. Type B
166 is massive, medium to fine black sand.

167 One kilometre from the first creek, “Diana waterfalls” creek crosses road N. 231 under a bridge (red
168 triangle L1 in Fig 1b). A lahar deposit is preserved at the foot of the waterfall, located 100 m upstream
169 from the road (Fig. 3b). In outcrop, the material appears to be remobilized Cordón Caulle 2011 tephra.
170 Figure 5b shows a stratigraphic section with a total thickness of 143 cm and 7 distinct beds of 3 different
171 lithofacies: C, D and E. Type C is a massive, pumice rich, coarse to fine gravel, clast supported deposit,
172 with some coarse sand. Type D is a massive, pumice rich, coarse sand with little fine gravel. Type E is
173 a massive, pumice rich, coarse sand to fine gravel, supported in a fine sand silty matrix.

174 Both lahar deposits from “Diana waterfalls” and “Road 231” are characteristic of hyperconcentrated
175 flows (Pierson, 2005) which, in our case, is a friable deposit with very little silt and clay. The lack of
176 large boulders in the deposit is another characteristic of hyperconcentrated flows.

177 Mud marks found on the top of the bridge (2m above the river bed) suggest the lahar reached the Blanco
178 River through the bridge.

179 At the same time lahars occurred in the Totoral basin, located approximately 7 km northeast of “Diana
180 waterfalls” creek (Fig. 1b). The lahars starting in channels on the valley slopes reached the main river,
181 causing bank erosion and overbank flows. Flooding and sediment deposition in the Totoral River valley
182 damaged houses in Paraje Rincón and destroyed trees (Fig. 4c and d).

183 On 10 June, floods were reported in Villa La Angostura. Remobilization of tephra-fallout on the channel
184 and hillslopes caused flooding and tephra accumulation in Villa La Angostura, which is situated on the
185 alluvial fan (Fig.1b).

186 At the end of the winter, on 19 September, a snow avalanche occurred in the Florencia river basin. The
187 avalanche, of volume $\sim 46000 \text{ m}^3$, started at the Florencia creek ridge crest and flowed approximately 1
188 km before stopping in the main river channel at 1200 m (Fauqué et al., 2011). Earlier observations in
189 the upper catchment had found a weakness between the lapilli bearing deposit (unit I and II) and the
190 snowpack. This discontinuity could have been the detachment surface of the slab avalanche. On 14
191 October, during the snow melting (spring), a natural dam, formed from previous lahars, broke in the
192 Colorado River, and increased the normal streamflow in the lower watershed (at Villa La Angostura
193 town) twofold.

194 Six months after the main eruption phase, a small lahar occurred in the Maderera Misiones catchment
195 and reached road N. 231. Has et al. (2012) reported two landslide scars in the upper catchment at 1400
196 m, and a natural dam that acted as a barrier and stopped the initial flow. The lahars initiated with the
197 dam break and flowed through the Maderera Misiones River into the lower catchment, reaching road N.
198 231. On route down to 1000 m, the flow incorporated material and logs from the river bed and deposited
199 lateral levees composed of tephra, boulders and logs. The flow cross section at 1000 m was estimated at
200 20 m^2 . The flow began to stop at the foot of the slope and the deposit here was estimated to be 10 m
201 across and 0.8 m high. The travel distance was approximately 2.3 km, but the total lahar volume was not
202 reported. On 30 January, after 113 mm of rainfall had accumulated in three days, floods and landslides
203 were reported in Villa la Angostura. The remobilization of volcanic material by surface water and in the
204 Las Piedritas River clogged the sewer, raising the water level and causing floods in the distal alluvial
205 plain (low area of the town).

206 Finally, starting on 2 June 2012, 223 mm rain fell in one week (Fig. 3b) causing several flood events in
207 the Villa La Angostura area. At the same time, heavy rain (120 mm in 24 hours measured at the Paraje
208 Rincon station, Fig. 3a) produced flooding in the Totoral drainage basin, damaging several houses
209 located in the alluvial plain. During our 2016 survey, we observed lahar-deposit levees in two small
210 channels of the catchment La Ponderosa at 1360 meters.

211

212 **3. Methods**

213

214 **3.1 Field campaign and data acquisition**

215 Three field campaigns were conducted to examine and collect samples in the lahar prone watersheds
216 near both the Chile-Argentina border and Villa La Angostura (Fig. 1b). Observations in the source areas
217 around Villa La Angostura were performed at separate intervals during the eruptive period. Due to
218 rugged terrain, narrow channel and dense vegetation, the upper catchments near the Chile-Argentina
219 border were inaccessible. The first campaign was in September 2011 (end of winter), the second in
220 November 2011 (spring), and the third in November 2016 (spring). During the 2016 field campaign we
221 collected 21 undisturbed tephra-fallout samples for geotechnical tests. Sampling was performed by
222 pushing a steel tube of height 15 or 30 cm (depending on the deposit thickness) and diameter 10 cm into

223 the ground. The samples were collected from preserved 2011 tephra fallout deposits in forested areas
224 near the “Diana waterfalls” watershed (Fig 1b, S1 and S2) and on the east hillslope of Cerro Bayo, at
225 1530 m (Fig. 1b, S3 and S4). We also make use of reports, photographs and oral communications by the
226 Villa La Angostura Civil Defence and Mountain Rescue group regarding lahar and flood events during
227 the volcanic eruption. Immediately after the main tephra fallout and during the following week,
228 volunteers from “Comité de montaña”, Civil Defence and SEGEMAR surveyed the upper catchment
229 collecting data from snow pits. Rainfall data, acquired from 3 rain gauges (Cerro Mirador, Rincón and
230 Villa La Angostura) for the period 2000-2015, has been provided by the Interjurisdictional Watershed
231 Authority from Neuquén Province (AIC). The stations are in the study area at altitudes between 700 and
232 1000 m on a west-east trend (Fig. 1b). All of the gauges supply daily rainfall. A geomorphological map
233 for 6 watersheds in Villa la Angostura was compiled in ArcGIS using on field data, satellite imagery
234 (Spot and Aster) and a digital elevation model (DEM). A DEM with a 10 m resolution provides the
235 topographic basis for the triggering modelling. The DEM was built from a stereo pair of satellite images
236 from World View 2, taken on the 24 December 2011 (CONAE, Argentina, 2011).

237

238 3.2 Slope stability models

239 Two stability models, namely SHALSTAB (Shallow Slope Stability Model; Montgomery and Dietrich,
240 1994) and TRIGRS (Transient Rainfall Infiltration and Grid-Based Regional Slope-Stability Model;
241 Baum et al., 2008) were applied to identify unstable areas along the slopes, and their results compared.
242 The test area comprises 2 upper catchments located in Villa La Angostura (Fig. 1b).

243

244 3.2.1 SHALSTAB model

245 SHALSTAB is a quantitative model for assessing topographic influence on shallow landslides,
246 combining a steady-state hydrological model with a simple slope stability model (Montgomery and
247 Dietrich, 1994). The authors use steady-state shallow subsurface flow equations, based on the work of
248 O’Loughlin (1986), to model hydrologic controls on h/z , where z is the soil depth, and h the water table
249 above the failure plane. The catchment is divided into topographic elements defined by elevation
250 contours orthogonal groundwater flow direction. The net rainfall (rainfall minus evapotranspiration) in
251 each topographic element becomes groundwater flow. The hydrological model thus reduces to the
252 calculation of a so-called wetness W , which is the ratio of local groundwater flux at a given steady state
253 rainfall to that at soil profile saturation

254

$$255 \quad W = \frac{qa}{bT\sin\beta}, \quad (1)$$

256

257 where q is the net rainfall intensity, a the upslope contributing area draining across b , which is the
258 cumulative drainage area of all topographic elements draining into an element, T soil transmissivity

259 when saturated, and β the local slope in (degrees) of the ground surface. The parameters a , b , and β are
 260 obtained from the DEM used in the analysis. There is a model assumption that for $W > 1$ excess water
 261 runs off as overground flow.

262 SHALSTAB is based on an infinite slope model including a Mohr-Coulomb soil failure criterion, which
 263 compares the destabilizing force of gravity, to the soil shear resistance forces of friction and cohesion
 264 along a failure plane parallel to the ground surface. Edge effects are neglected (Tarolli and Tarboton,
 265 2006).

266 Initially, Montgomery and Dietrich (1994) considered cohesion c to be zero, which is realistic for air-
 267 fall cohesionless volcanic materials. After neglecting cohesion, the infinite slope stability model can be
 268 solved for h/z , which is the proportion of the soil column that is saturated at failure

269

$$270 \quad \frac{h}{z} = \frac{\rho_s}{\rho_w} \left[1 - \frac{\tan\beta}{\tan\phi} \right], \quad (2)$$

271

272 where ρ_s and ρ_w are the soil and water bulk density respectively and ϕ is the soil friction angle.

273 Combining the slope stability hydrological models (Eqs. 1-2), we obtain the critical steady-state
 274 precipitation event q/T required to cause instability for cohesionless soils

275

$$276 \quad \frac{q}{T} = \left(\frac{b \sin\beta}{a} \right) \left(\frac{\rho_s}{\rho_w} \right) \left[1 - \frac{\tan\beta}{\tan\phi} \right]. \quad (3)$$

277

278 Later, Montgomery et al. (1998) provided the equation for the case of soils with cohesion and the q/T
 279 required to cause instability is

280

$$281 \quad \frac{q}{T} = \left(\frac{b \sin\beta}{a} \right) \left[\frac{c'}{\rho_w g z \cos^2\beta \tan\beta} + \frac{\rho_s}{\rho_w} \left(1 - \frac{\tan\beta}{\tan\phi} \right) \right] \quad (4)$$

282

283 Further details for the model with cohesion can be found in Montgomery et al. (1998). Both model with
 284 and without cohesion have been used in this work.

285 SHALSTAB classifies landslide susceptibility as: “unconditionally stable”, “potentially unstable” and
 286 “unconditionally unstable”. Slopes that are stable even when $W=1$ (wet) are classified as unconditionally

287 stable, and excess pore pressure is needed to generate slope instability. Similarly, slopes predicted to be
 288 unstable even when dry ($W=0$) are unconditionally unstable. Landslide susceptibility is calculated using

289 equations 3 and 4, obtaining a range of values for q/T . Since T is much greater than q , q/T is very small,
 290 meaning it is helpful to convert these values to $\log(q/T)$, which are found to range from -10 and 10.

291 Then, a range of $\log(q/T)$ is defined for each landslide susceptibility class. Critical rainfall values can
 292 be calculated for each class, if the transmissivity is estimated. A fundamental premise of the model is

293 that areas found to have the lowest q/T values (least amount of precipitation required) represent the least

294 stable areas and have the greatest potential for shallow landslides. Thus, the general scope of such
 295 analysis is to attribute the q/T values as “instability descriptors” to each single cell of the DEM (Digital
 296 Elevation Model).

297

298 3.2.2 TRIGRS model

299 The Fortran Program TRIGRS was developed by Baum et al. (2002) for computing transient pore
 300 pressure changes and subsequent changes in safety factors due to rainfall infiltration. They extended the
 301 method of Iverson (2000) by implementing a complex time sequence of rainfall intensity, an
 302 impermeable basal boundary at infinite depth and an optional unsaturated zone above the water table
 303 (Baum et al. 2002). They also, added a simple runoff-routing scheme to disperse excess water from cells
 304 where the rainfall intensity exceeds the infiltration capacity, according to the vertical Darcy flow
 305 velocity (product of soil conductivity and vertical hydraulic gradient), where “the infiltration (I) at each
 306 cell is the sum of precipitation (P) plus any runoff from upslope cells (R_u). When $P+R_u$ exceeds K_{sat} , the
 307 excess is considered runoff and is diverted to upslope adjacent cells”. TRIGRS combines models for
 308 infiltration and groundwater flow due to rainfall, routing of runoff, and slope stability to calculate the
 309 effects of storms on the stability of slopes over large areas.

310 The infiltration models in TRIGRS for wet initial conditions are an extension of Iverson’s (2000)
 311 linearized solution of the Richards equation for Darcian flow of groundwater in response to rainfall on
 312 the slope (Baum et al., 2002; Savage et al., 2003, Savage et al., 2004). The solution is valid only where
 313 transient infiltration is vertically downward and transient lateral flow is relatively small. The equation
 314 for the transient vertical groundwater flow is

315

$$316 \quad \frac{\partial \psi}{\partial t} C(\psi) = \frac{\partial}{\partial z} \left[K(\psi) \left(\frac{\partial \psi}{\partial z} - \sin \beta \right) \right], \quad (5)$$

317

318 where ψ is the pressure head, $K(\psi)$ is the pressure- head dependant hydraulic conductivity, $C(\psi) = d\theta/d\psi$
 319 is the specific moisture capacity, θ is the volumetric water content, β is the slope angle of the ground
 320 surface, and Z is the vertical depth (Philip, 1991). For wet initial conditions the pressure dependent
 321 quantities $K(\psi)$ and $C(\psi)$ become constant values, K_{sat} and C_0 , where C_0 is the minimum slope of the soil
 322 water retention curve, which is the relationship between θ matric suction used to describe unsaturated
 323 soil behaviour (Fredlund and Xing 1994). Equation 5 then reduces to a linear diffusion equation

324

$$325 \quad \frac{\partial \psi}{\partial t} = D_1 \frac{\partial^2 \psi}{\partial z^2}, \quad (6)$$

326 where $D_1 = D_0 / \cos^2 \beta$ and $D_0 = K_{sat} z / C_0$.

327 An analytical solution to Eq. (6) is proposed by Baum et al. (2002) and implemented in a Fortran code.
 328 Additionally, TRIGRS is applicable to unsaturated initial conditions with a two layer system consisting
 329 of a saturated zone with a capillary fringe above the water table, overlain by an unsaturated zone

330 extending to the ground surface. The unsaturated zone acts like a filter that smoothes and delays the
 331 surface infiltration signal at depth. The model utilises the soil-water characteristic curve for wetting of
 332 the unsaturated soil as proposed by Gardner (1958) and approximates the infiltration process as one-
 333 dimensional vertical flow (Srivastava and Yeh, 1991, Savage et al., 2004).

334 Following Iverson (2000), slope stability is calculated using an infinite-slope stability analysis. Incipient
 335 failure of infinite slopes is described by an equation that balances the downslope component of
 336 gravitational driving stress against the resisting stress due to basal Coulomb soil friction, incorporating
 337 the influence of groundwater (Iverson, 2000). The Factor of Safety (FS) is calculated at a depth Z by
 338

$$339 \quad FS(Z,t) = \frac{\tan\phi'}{\tan\beta} + \frac{c' - \psi(Z,t)\gamma_w \tan\phi'}{\gamma_s Z \sin\beta \cos\beta} \quad , \quad (7)$$

340
 341 where t is time, c' is the effective soil cohesion, ϕ' the effective friction angle, γ_w is the unit weight of
 342 groundwater and γ_s is the unit weight of soil. The pressure head $\psi(Z, t)$ in (7) is obtained from various
 343 formulae depending on the particular conditions modelled.

344 FS is calculated for pressure heads at multiple depths (Z). The slope is predicted to be unstable where
 345 $FS < 1$, in a state of limiting equilibrium where $FS=1$ and stable where $FS > 1$. Thus, the depth Z of
 346 landslide initiation is where FS first drops below 1.

347
 348 **3.2.3 Simulation parameters, slope stability scenarios and comparison with field data**

349 We chose two representative upper basins (Colorado and Florencia), where the recent tephra-fallout
 350 deposit located on the bare slopes were partially remobilised by shallow landslides, as locations where
 351 to apply the SHALSTAB and TRIGRS models.

352 For both SHALSTAB and TRIGRS, the thickness of the tephra-fallout deposit was taken to be 15 cm,
 353 in agreement with the corresponding isopach map (Fig. 1a) (Pistolesi et al., 2015). However, the tephra-
 354 fallout deposit in this area consists of two very different layers with contrasting grain sizes: Unit I+II,
 355 and Unit III of Pistolesi et al. (2015). In Villa La Angostura (48 km from vent) the typical sequence is a
 356 5 cm upper ash layer, with a median grain diameter of 0.25 mm (Unit III), and a 10 cm lower layer with
 357 a median grain diameter of 1 mm (Unit I and II). As the model SHALSTAB and TRIGRS are designed
 358 for homogenous deposits or soil, the modelled tephra-fallout deposit was simplified, and two different
 359 scenarios were considered. The first scenario (S1) considers a homogenous ash layer of 15 cm (i.e.
 360 Unit I+II+III) (Fig. 4). For the second scenario (S2), we considered a 10-cm thick lapilli layer (Fig. 6).
 361 For locations 28 km from the vent area we used a tephra-fallout deposit thickness of 30 and 20 cm for
 362 scenarios 1 and 2 respectively.

363 The soil mechanical features, as well as the slope angle are reported in Tab. 1-2. Hydraulic conductivity
 364 (K_{sat}) for lapilli was measured in the field by filling a plastic tube with an undisturbed sample and
 365 saturating the material with water. We then measured the time taken for the water to drain to estimate

366 the hydraulic conductivity (Tab. 2). As long term and short-term pressure head responses can be
367 described with the simplified forms of Richards equations, where the ratio $\alpha = z/\sqrt{a} \ll 1$, we obtained
368 the upslope contributing area (a) for the lahar source zones using Taborton's (1997) $D - \infty$ algorithm
369 and calculated α for a depth of 0.15 m. Values of α are between 0.015 and 0.004.

370 For initial conditions in TRIGRS, we considered the water table to be located at the bottom of the tephra
371 sequence (lower boundary) and an impermeable layer below the tephra sequence, which were emplaced
372 on cretaceous rock outcrops, debris mantled slopes and volcanic soils.

373 The rainfall intensity I was determine according to daily rainfall data from the "Villa La Angostura"
374 station (AIC, Autoridad Interjurisdiccional de Cuencas, 2016). The provided rainfall data were daily
375 totals. Therefore, in order to test the effect of different rainfall intensities on landslide processes in the
376 upper catchment, we ran (with TRIGRS) both scenarios for three different rainfall duration and
377 intensities (Tab. 3). Since parts of the upper basin areas are forested, mainly by *Nothofagus pumilio*, a
378 fraction of the rainfall is intercepted by the canopy. We thus considered a rain interception of 25 %
379 based on the study of Martinez Pastur et al. (2011). The rainfall intensities for both bare soil area and
380 forested area are given in Tab. 3. For SHALSTAB, a critical rainfall intensity of 5 mm/day was
381 considered, corresponding to the mean rainfall intensity for 2011 (Sorbino et al., 2010).

382 To investigate the sensitivity of TRIGRS to cohesion variations in scenario 1, we perform calculations
383 for cohesion values between 0 and 1.5 kPa, for two different tephra thicknesses 0.15 m and 0.30 m (Fig.
384 7). As the result obtained with zero cohesion for scenario 1 overestimated the unstable area (80% for
385 0.15 m thickness, 46% for 0.3 m), we took cohesion to be equal to 0.5 kPa for the soil thickness of 0.15
386 m and 1 kPa for 0.30 m.

387 The results from the different models and scenarios were compared with the field observations collected
388 during the eruption and 5 years later in the upper catchment Florencia. Particularly, we measured the
389 2011 tephra sequence in the different geomorphologic units and described the remobilization by rill
390 erosion and shallow landslides. Based on field observation, measurements of 2011 tephra deposits and
391 description on remobilization by rill erosion and shallow landslides, a map of the observed lahar source
392 areas was created for the Florencia river upper catchment. Finally, the unstable volume for of bare soil
393 area was calculated in each case.

394 Three metrics are used to compare the observed and simulated lahar source areas: the Jaccard similarity
395 coefficient (Levandowsky and Winter, 1971), and two metrics derived from Bayes' Theorem, model
396 sensitivity and model precision (Charbonnier et al., 2018).

397 We quantified the quality of model fitting to the field evidence through the Jaccard similarity coefficient
398 (R_j) (Kubanek et al. 2015) by dividing the intersection of the observed source areas A_{obs} and unstable
399 modelled areas A_{sim} by their union. Observed source areas determined unstable by the model ($A_{obs} \cap$
400 A_{sim}) are classified as true positive (TP), and those computed as unstable by the models, but not observed
401 as source areas are false positive (FP). Conversely, observed source areas that are simulated to be stable
402 are false negative (FN) and true negative (TN) areas are those observed to be stable in reality and the

403 simulation (Fig. 8).

404 The Jaccard similarity coefficient is

$$405 R_J = \frac{|A_{obs} \cap A_{sim}|}{|A_{obs} \cup A_{sim}|} \times 100 = \frac{TP}{TP + FN + FP} \times 100 \quad (8)$$

406 Charbonnier et al. (2018) identified the similarity of R_J to Bayes' Theorem, which describes the
407 probability of predicted unstable areas, based on the observed source areas and vice-versa. Bayes'
408 Theorem serves as link between simulated and observed unstable areas

$$409 P_r(A_{obs}/A_{sim})P_r(A_{sim}) = P_r(A_{sim}/A_{obs})P_r(A_{obs}), \quad (9)$$

410 where, $P_r(A_{obs})$ is the probability that an area is unstable according to observations, $P_r(A_{sim})$ the
411 probability that an area is unstable according to the model, $P_r(A_{sim}/A_{obs})$ the conditional probability
412 of A_{sim} given A_{obs} and $P_r(A_{obs}/A_{sim})$ the conditional probability of A_{obs} given A_{sim} . Rearranging
413 equation 9, we obtain

$$414 P_r(A_{obs}/A_{sim}) = \frac{P_r(A_{sim}/A_{obs})P_r(A_{obs})}{P_r(A_{sim})}. \quad (10)$$

415 We identify $P_r(A_{obs}/A_{sim})$ as the model precision and $P_r(A_{sim}/A_{obs})$ as the model sensitivity. Combing
416 Eqs. 8 and 10, we obtain

$$417 R_{MP} = \frac{|A_{obs} \cap A_{sim}|}{|A_{sim}|} \times 100 = \frac{TP}{TP + FP}, \quad (11)$$

418 and

$$419 R_{MS} = \frac{|A_{obs} \cap A_{sim}|}{|A_{obs}|} \times 100 = \frac{TP}{TP + FN}. \quad (12)$$

420 A high model precision R_{MP} indicates a good match between the model predicted and observed unstable
421 areas, without taking into consideration observed unstable areas not simulated by the model. The model
422 sensitivity R_{MS} gives the percentage of lahar source areas that the model correctly predicts, without
423 counting the FP areas. A model simulation with high sensitivity agrees well with the observed source
424 areas, but may predict unstable areas outside the observed sources.

425

426 4. Results

427

428 4.1 Geomorphology of the study area and field observations

429 4.1.1 The watersheds of Villa La Angostura

430 Villa La Angostura is situated on an alluvial fan, at the convergence of six watersheds: Las Piedritas,
431 Colorado, Florencia, La Ponderosa, Maderera Misiones and El Muerto. Fig. 9 shows the
432 geomorphological map of all the watersheds.

433 The Las Piedritas River upper catchment is a U-shaped valley with steep lateral hillslopes. The river

434 originates at an elevation of 1450 m in an old glacial cirque and runs through the valley until 1090 m.
435 At this point, the river makes a 60 m jump (waterfall) and flows through a granitic canyon for almost
436 0.6 km before reaching the alluvial fan. The river runs between small hills to the south, before crossing
437 Villa La Angostura and reaching the Nahuel Huapi Lake. The Colorado River also originates in a small
438 glacier cirque, at an elevation of 1650 m, and is fed by many first order channels which drain the back
439 and lateral upper catchment slopes (talus debris slope and forested hillslopes). The upper Colorado basin
440 has an old cirque front slope, with many small channels draining the area. Below 1250 m the stream
441 flows through a narrow valley with several cascades and reaches the lower catchment at 890 m, near the
442 Villa La Angostura water plant. The Florencia upper catchment is a small glacial cirque with steep slopes
443 and debris flow prone channels. The river in the middle catchment is confined and has several waterfalls
444 before reaching the lower catchment and run into the Colorado River. The back and lateral hillslopes
445 have been divided in three main geomorphological units: rock outcrops, talus debris slopes and forested
446 hillslopes. Two debris-flow prone channels have been mapped, one in the Florencia and the second in
447 Colorado upper catchment. The summit and valley interfluves are glacially smoothed, with plane and
448 gentle slopes between 0° and 15°. The middle watershed is located on the regional Nahuel Huapi valley
449 flank. The proximal alluvial fan area has glacial erosional landforms and 10 m high elongated hillslopes
450 with some swamps areas filled with volcanic sediments. The distal alluvial fan is flat marshland crossed
451 by the Piedritas River, which splits into at least two channels before reaching the Nahuel Huapi Lake.
452 The La Ponderosa, Maderera Misiones and El Muerto watersheds drain the southern Cerro Bayo flank
453 (Fig. 1b). The upper catchment source area has steep slopes between 15° and 45° and range in area from
454 0.153 km² (La Ponderosa) to 0.62 km² (Madera Misiones). The uppermost part of the hillslopes pertains
455 to the Cerro Bayo ski field and has been modified with a manmade track.

456

457 4.1.2 Shallow landslides and erosion in the lahar source areas

458 Examination of the upper catchment of Villa La Angostura in spring (November 2011) found different
459 types of erosion and remobilization. Rills formed just below the crest, at slope angle of 25-35°, and
460 below rock outcrops located on the top or middle hillslope (Fig. 6d). Rills formed were erosion was
461 focused by flow-concentrating irregularities, such as boulders (Horton, 1945, Mannville et al., 2000),
462 on the talus debris slope unit. Otherwise shallow landslides occurred where the tephra deposit was lying
463 either on outcropping rock or the steep talus debris slope (Fig. 9d). The tephra was mobilized into first
464 order drainage concavities (Fig. 9e), located on the talus debris slope. Measurements, on these mobilized
465 deposits, performed in November 2011, found a 15 cm primary tephra fall deposit and 15 cm of
466 remobilized tephra.

467 Observations from December 2016 in the upper catchment of Florencia and Colorado, showed that the
468 2011 tephra deposit was almost completely eroded from the rock outcrops and bare hillslope since the
469 old black tephra deposit cropped out in many hillslope areas, as before the 2011 eruption. Nevertheless,
470 a small fraction of tephra forms the debris slope colluvium, which is a mix of tephra and rock boulders.

471 Part of the eroded tephra remains in the first order channels. Figure 10 shows the tephra deposit erosion
472 stage in the Florencia upper catchment between June 2011 and December 2016. Tephra was first
473 removed from rock outcrops, which represent 22% of the whole upper catchment (Fig. 10b). At the same
474 time tephra from hillslopes (31%) was partially removed by rill erosion, shallow landslides and
475 downslope creep mostly related to snowmelt during the spring (Fig. 10b). Five years later, tephra was
476 almost completely removed from rock outcrops and unforested hillslopes. Part of the eroded sediment
477 remained in the first order channel and in the forested areas which represent 8% and 39% of the upper
478 catchment, respectively (Fig. 10c). The tephra sequence was well preserved on the forested hillslopes.

479

480 **4.2 Modelling**

481 Instability scenarios modelled with SHALSTAB for two upper watersheds (Colorado River and
482 Florencia River) in Villa La Angostura are presented here. Figure 11 shows two maps with different
483 levels of instability computed with the SHALSTAB model (scenario 1, Tab, 1). Figures 11a and 11b
484 show the results without and with cohesion respectively. We defined four stability descriptors:
485 unconditionally unstable, unstable, stable, unconditionally stable. The results for scenario 1 with a
486 critical rainfall (q) of 5 mm/day are presented in Tab. 4. We also ran SHALSTAB for scenario 2, but
487 the amount of rain needed for instability is out of range, between 202 and 6000 mm/day, 40 and 1200
488 times the critical rainfall value calculated for the study area respectively. In this case the unconditionally
489 unstable area represents approximately 1% of the total upper catchments.

490

491 Figures 12 and 13 illustrate the evolution of unstable areas for the Colorado and Florencia Rivers upper
492 watersheds through time calculated with TRIGRS for scenarios 1 and 2. The colour lines represent three
493 different rainfall intensities and durations (Table 3). Figures 12a, b and 13a, b show that for scenario 1,
494 a maximum fraction of unstable area was attained for all three rainfall intensities. Conversely for scenario
495 2, the maximum fraction was only reached for the greatest rainfall intensity (3.3 mm/h). It is also seen
496 that more time is needed to reach the maximum unstable area when the tephra thickness is doubled (0.30
497 m). This modified slope response depends on the transient groundwater response time Z^2/D_0 . This
498 timescale is the minimum time necessary for slope-normal pore pressure to transmit from the ground
499 surface to depth Z (Iverson and Major, 1987; Haneberg 1991; Reid, 1994). Comparing results for the
500 Colorado upper watershed (Figs. 12 a-d) with the Florencia upper watershed (Figs. 13 a-d) both show
501 qualitative agreement for the different scenarios and tephra thicknesses, but there is much greater
502 potential for unstable areas in the Florencia study case. This large difference is due to the different
503 topography, since slope angles between 38.4° and 53° cover only 6% of the Colorado upper basin area,
504 but 20% in the Florencia upper basin. Table 5 lists all of the values of unstable area percentage as
505 calculated with TRIGRS for the Colorado River and Florencia River upper catchments.

506 Model validation metrics (R_J , R_{MP} and R_{MS}) calculated for the upper catchment Florencia River using
507 both TRIGRS and SHALSTAB are given in Table 2. For scenario 1 (Ash deposits), both SHALSTAB

508 (without cohesion) and TRIGRS give the highest Jaccard similarity coefficient, $R_J = 48\%$ and 47% ,
509 respectively. These simulations also have high model sensitivities. For scenario 2 (lapilli deposits) the
510 highest R_J was achieved for the highest rainfall intensity and a duration of 24h.
511 TRIGRS model S1 determined most of the source areas to be in the bare soil areas (Fig. 14b), but also
512 predicted a lot of the forested stable areas to be unstable (FP). This is reflected in the model precision
513 (57%). Figure 14c shows that for the case of the lapilli deposits (scenario 2) and 24h of rainfall, the
514 model underestimated the fraction of observed source areas, but was more accurate in the forested stable
515 areas ($R_{MS} 62.9\%$). Finally, the unstable volumes in both bare soil upper catchment areas, as calculated
516 from the best fit scenario, are presented in Tab. 7.

517

518

519 **5. Discussion**

520

521 **5.1 Remarks on modelling results**

522 The direct investigation of the lahar source areas of the 2011 eruption of Cordón Caulle provided
523 invaluable insights into lahar triggering mechanisms and the amount of remobilised tephra. Tephra-
524 fallout properties (friction angle, hydraulic conductivity and diffusivity) required by numerical models
525 and obtained for the ash and lapilli sequences around Cordón Caulle, represent the first data derived for
526 this region. The 2011 tephra-fallout stratigraphy, with 2 contrasting layers (ash and lapilli), is too
527 complex to be analysed with the SHALSTAB and TRIGRS models, which are designed for homogenous
528 deposits. We therefore considered, two different scenarios. Comparing the two models, we found that
529 TRIGRS provides an estimation of the timing (based on a storm event) and location of a potentially
530 unstable area, while the topographic effects on shallow landslides can be determined with SHALSTAB.
531 For both models, results are sensitive to the physical properties of the tephra-fallout sequence and thus
532 require accurate knowledge of the hydraulic and material strength properties at the scale of catchment
533 area. TRIGRS requires additional parameters such as hydraulic diffusivity and information on initial
534 water table. The results obtained with TRIGRS demonstrate that shallow landsliding is possible in our
535 study area for both ash and lapilli bearing sequences. However, the ash sequence (scenario 1), with the
536 low permeability and diffusivity, has a higher predisposition for instability compared with the high
537 permeability and diffusivity lapilli sequence (scenario 2). The same maximum unstable areas are found
538 for the 3 different storms in the case of ash sequences (S1), but the time needed to reach the maximum
539 is different. For the lapilli sequences (S2), the unstable area percentage decreases as the rainfall intensity
540 decreases, and the unstable area percentage increases with time.

541 Only having daily rainfall data, instead of more detailed hourly data, was a limitation for the simulations
542 because the relationship between rainfall intensity (I) and hydraulic conductivity (K_{sat}) determines the
543 behaviour of pressure head response. The time required to develop positive pressure and further

544 instability ($FS < 1$) decreases with rainfall intensity, as demonstrated in Figs. 12 and 13 where the rate of
545 growth of the unstable area is faster for higher rainfall intensity. Therefore, we tested different rainfall
546 intensities and duration according to daily rainfall data in the study area.

547 As we already described in section 3.1.2, we did not observe shallow landslides in the 2011 tephra
548 deposit on the forested hillslope. For the TRIGRS model we accounted for rain interception (25%) in
549 forested areas, but still prediction many unstable areas, which did not match with observations. There
550 are many reasons for the reduction of shallow landslides in forested areas: root strength,
551 evapotranspiration, evaporation and preferential drainage via root systems (Phillips and Watson, 1994;
552 Sidle and Ochiai, 2006). In our case the tree and litter roots at the base of the tephra deposit could have
553 enhanced the drainage and thus dissipate positive pore water pressure in the tephra section (Uchida et
554 al., 2001). Several months after deposition, a new litter of leaves and new plants growing on the tephra
555 deposits further reduced the potential for shallow landslides and sheet erosion.

556

557 **5.2. Comparison with previous lahar-triggering models**

558 Coupled hydrological and infinite-slope models have previously been used by several authors (Frattini
559 et al., 2004; Sorbino et al., 2007; Cascini et al., 2011) to perform spatially distributed simulations of the
560 catastrophic landslides and flow events of Sarno, 1998. The pyroclastic deposits in the landslide source
561 areas (above Sarno town) consisted of pumice lapilli clasts and ashy layers belonging to at least 5
562 different eruptions from Somma-Vesuvius volcano. Frattini et al. (2004) used a lateral flux model for
563 kinematic subsurface storm flow and a vertical flux was simulated through a simplified formulation
564 derived from Richard's equation (Iverson 2000). The results showed that both vertical and lateral fluxes
565 were responsible for landslide triggering. In our study, the results from SHALSTAB demonstrated that
566 lateral fluxes were responsible for instabilities in ash layers (S1), but not for lapilli layers (S2). Sorbino
567 et al. (2007) applying the physically based models SHALSTAB, TRIGRS and TRIGRS unsaturated,
568 show that the most adequate model for analysis of shallow landslide source area in Sarno was TRIGRS
569 unsaturated. Our result instead indicates that TRIGRS and SHALSTAB models both produced good
570 results for ash layers, but the best model for the lapilli layers was TRIGRS.

571 Additional strategies for studying lahar triggering exist. For example, Volentik et al. (2009) analysed
572 the potential hazard of lahars to the Bataan nuclear power plant site (Philippines), focusing on the nature
573 of tephra fallout and lahar generation. They used the slope stability model, based on an infinite slope
574 form of the Mohr Coulomb failure criterion following Iverson (2000), to calculate the potential for
575 gravitationally induced failure of the tephra deposit on the volcano slopes, thus triggering lahars. The
576 main difference with TRIGRS (which accounts for transient rainfall effects) is that Volentik et al. (2009)
577 considered the effect of rainfall infiltration on the pressure head, with results from a static infinite slope
578 analysis assuming two water table conditions. If we were to use the Volentick et al. (2009) model for
579 the case of an ash layer (scenario 1), the percentage of unstable area would have been similar, but for a
580 lapilli layer the model would have overestimated the unstable area. The main reason for this is that the

581 model does not consider the deposit hydraulic conductivity and the amount of rain needed to saturate it.
582 In the case of a probabilistic lahar-hazard assessment, with no information on hydraulic conditions and
583 tephra-fallout properties at the scale of lahar processes, the choice of a simple slope stability model to
584 calculate potential lahar source region was appropriate.

585 Mead et al. (2016) also carried out an interesting study on rain-triggered lahar susceptibility using
586 shallow landslide and erosion models. They used the model developed by Iverson (2000) with an infinite
587 slope failure criterion and the reduced form of the Richard's equation. Their shallow landslide and
588 erosion models were applied to the 1995 lahar of Ruapehu volcano, New Zealand. Here, the volume of
589 material remobilised from the Mangatoetoeu glacier was known and the lahar well documented, but
590 the hydraulic properties and depth of ash deposits were unknown. Different scenarios were modelled
591 with the slope stability model, varying diffusivities and infiltration rates to calculate landslide material
592 volume estimates which were compared with the observed volume of the Mangatoetoeu lahar in order
593 to choose the best hydraulic parameters. The main difference between the approach of Mead et al. (2016)
594 and our strategy is that we compare different slope stability models (TRIGRS and SHALSTAB) and
595 two different tephra layers for the estimate of lahars initiation volumes, while Mead et al. (2016)
596 combined a slope stability model with an erosion model to calculate the lahar initial volume.

597

598 **5.3. Implication for the compilation of lahar-hazard maps**

599 During the first 6 months of the 2011 eruption of Cordón Caulle, an estimate of the unstable tephra-
600 fallout volume in the Villa La Angostura upper catchments was made by the Argentinian Geological
601 Survey (SEGEMAR), assuming that 100% of the unforested, fallout covered areas would be eroded.
602 These estimates were used by Córdoba et al. (2015) to calculate the runout and thickness of a potential
603 lahar event in Villa la Angostura. They assumed 75% and 90 % of the deposited tephra as a high initial
604 volume for the Colorado and Florencia upper catchment respectively. Our simulation results for the
605 same bare soil upper catchments were similar with SHALSTAB and lower with TRIGRS both for ash
606 layer (Table 7). In the case of Colorado bare soil upper catchment TRIGRS model simulated that only
607 27.2% and 12.9% would be unstable for scenario 1 and scenario 2 respectively (Table 7).

608 An evaluation of potential mobilised volumes is fundamental to the modelling of both lahar spreading
609 and inundation that is required for the compilation of lahar-hazard maps. Our results demonstrate the
610 importance of using physical models (e.g. TRIGRS) combined with geotechnical data (when available)
611 so to provide accurate estimates of remobilised tephra volumes. Our results also show the potential of
612 using the SHALSTAB and TRIGRS models to predict the solid fraction of a lahar triggered by rainfall.
613 As an example, our new data on rain-triggered lahars for the 2011 eruption of Cordón Caulle can be
614 used as input for lahar-hazard assessments. The results obtained with shallow landslide models using
615 rainfall intensity, duration and frequency thresholds (IDF), could be used to create a rain-triggered lahar
616 susceptibility map (Mead et al., 2016). To assess the lahar hazard we could combine the unstable area
617 results for variable rainfall IDF (rain triggered lahar susceptibility map) with a lahar run-out model. The

618 total unstable area in each river upper catchment is the potential mobilised sediment volume used as
619 input in lahar run-out models. In addition, the evaluation of unstable area obtained with physically based
620 models such as TRIGRS or SHALSTAB provide important inputs for compiling dynamic lahar-hazard
621 maps of long-lasting eruptions, that can be adapted through time according to the varying eruptive
622 dynamics (variation of tephra thickness and grain size, rainfall, etc.).

623

624 **6. Conclusions**

625 We have presented a detailed analysis of rain-triggered lahars combining geomorphological
626 observations and geotechnical data with numerical studies based on two slope-stability models:
627 SHALSTAB and TRIGRS. We applied our methodology to events that occurred after the main phase of
628 the 2011 eruption of Cordón Caulle volcano, Chile. SHALSTAB mostly describes topographic influence
629 on shallow landsliding, while TRIGRS accounts for rain infiltration to assess unstable areas. Due to the
630 heterogeneity of the tephra-fallout deposits that generated the lahars (i.e. combination of ash and lapilli
631 layers), different initial conditions have been tested. Tests consisted of two main scenarios with different
632 soil and hydraulic parameters. In addition, different rainfall intensities and durations and two values of
633 tephra-fallout thicknesses have been used in TRIGRS for the analysis of shallow landsliding. The
634 comparison between field observations and model outcomes shows that:

635 1) both SHALSTAB and TRIGRS provide a goodness of fit of nearly 50% for ash layers (scenario 1)
636 and also a high model sensitivity. The SHALSTAB model for lapilli layers (scenario 2) was not realistic,
637 but scenario 2 simulated with TRIGRS had a fit of 40 % and high precision in the case of high rain
638 intensity;

639 2) results from both models are sensitive to the physical properties of the tephra-fallout deposit and to
640 the hydraulic properties and strength of the material in the study area. TRIGRS requires more parameters
641 than SHALSTAB, such as hydraulic diffusivity and information on initial water table;

642 3) TRIGRS provides estimates of the timing (based on a storm event) and location of a potentially
643 unstable area, while SHALSTAB provides landslide susceptibility classes based on critical rainfall
644 values.

645

646 The comparison between the different scenarios modelled with TRIGRS shows that:

647 1) an increase in rainfall intensity increases the extent of unstable areas for lapilli layers (scenario 2).
648 Conversely, the extent of unstable areas is not affected by rainfall intensities for ash layers (scenario 1);

649 2) the time taken for positive pore pressure to develop is larger for larger values of tephra-fallout
650 thickness (ground surface to depth H) and depends on the transient groundwater response time H^2/D_0 .

651 The shallow landsliding process modelled with SHALSTAB and TRIGRS provides important data of
652 lahar initiation processes from recent tephra fallout sequences, emphasising in particular the importance
653 of considering the presence of different ash layers and associated geotechnical data in the susceptibility
654 of a slope.

655
656
657
658
659
660
661
662
663
664
665
666
667
668
669

Acknowledgments

The authors are grateful to M. Elissondo, M. Pistolesi, R. Cioni, Meier, L. Piantanida, D. Villegas, L. Fauqué and J. González for their support and discussion in the field and A. Napoli and C. De Conciliis for the help with the use of the model TRIGRS. We also acknowledge the funding support of the Société de Physique et d’Histoire Naturelle de Genève (SPHN) and of the Swiss National Science Foundation (#200021_163152) and the logistic support of the SEGEMAR (Servicio Geológico y Minero Argentino). The Argentinian Aerospace Agency (CONAE) is thanked for providing the DEM and the AIC (Autoridad Interjurisdiccional de las Cuencas de los ríos Limay, Neuquén y Negro) for providing rain data. The laboratory tests were performed at the Laboratory of Geotechnics of University of Salerno (Italy) within the framework of different projects: FARB 2015 “Laboratory testing and constitutive modelling of unsaturated soils”; FARB 2016 “Multiscale analysis of the mechanical behaviour of unsaturated soils” funded by the Italian Education and Research Ministry; 2014-2020 Erasmus+ European Project.

671 **Appendix A**

672

673 Notation

674

| Symbol | Description | Units |
|------------------|--|----------------------|
| a | upslope contributing area | m ² |
| b | grid cell width | m |
| c | cohesion | kPa |
| c' | effective soil cohesion | kPa |
| C (ψ) | moisture capacity | 1/kPa |
| D ₀ | hydraulic diffusivity | m ² /s |
| d | depth of the steady state water table | m |
| d _{lb} | vertical depth to the lower boundary | m |
| FS | factor of safety for a hillslope | |
| h | water level above the failure plane | m |
| I _z | long term (steady state) rainfall flux at the ground surface | mm/h |
| K | hydraulic conductivity | m/s |
| K _{sat} | saturated hydraulic conductivity | m/s |
| K _Z | hydraulic conductivity in the Z direction | m/s |
| q | net rainfall rate | mm/day |
| T | soil transmissivity | m ² /s |
| W | wetness | |
| z | soil depth | m |
| Z | depth of landslide initiation | m |
| β | local slope | deg |
| φ | angle of internal friction | deg |
| φ' | affective angle of internal friction | deg |
| ρ _s | soil bulk density | tonne/m ³ |
| ρ _w | water bulk density | tonne/m ³ |
| γ _s | unit weight of soil | kN/m ³ |
| γ _w | unit weight of water | kN/m ³ |
| □ | ground-water pressure head | kPa |
| θ _s | saturated volumetric water content | % |
| θ _r | residual volumetric water content | % |
| α | pore size distribution index; SWCC modeling constant | |
| □ | Time scale ratio | |

675

676

677

678

679

680 **References**

681 AIC (Autoridad Interjurisdiccional de las Cuencas de los ríos Limay, Neuquén y Negro), 2016.

682 www.aic.gov.ar

683 Barclay, J., Alexander, J., Susnik, J., 2007. Rainfall-induced lahars in the Belham Valley, Montserrat,
684 West Indies. *J. Geol. Soc. London.* 164, 815–827. <https://doi.org/10.1144/0016-76492006-078>

685 Baum, R. L., Savage, W. Z., Godt, J. W., 2002. TRIGRS—a Fortran Program for Transient Rainfall
686 Infiltration and Grid-Based Regional Slope-Stability Analysis. US geological survey open-file
687 report, 424, 38.

688 Baum, R. L., Savage, W. Z., Godt, J. W., 2008. TRIGRS — A Fortran Program for Transient Rainfall
689 Infiltration and Grid-Based Regional Slope-Stability Analysis, Version 2.0. U.S. Geological
690 Survey Open-File Report, (2008–1159), 75. <https://doi.org/Open-File Report 2008–1159>

691 Caballero, L., Capra, L., 2014. The use of FLO2D numerical code in lahar hazard evaluation at
692 Popocatepetl volcano: A 2001 lahar scenario. *Nat. Hazards Earth Syst. Sci.* 14, 3345–3355.
693 <https://doi.org/10.5194/nhess-14-3345-2014>

694 Caballero, L., Capra, L., Vázquez, R. (2016). Evaluating the Performance of FLO2D for Simulating Past
695 Lahar Events at the Most Active Mexican Volcanoes: Popocatepetl and Volcán de Colima. *Natural
696 Hazard Uncertainty Assessment: Modeling and Decision Support*, 223, 179.

697 Capra, L., Borselli, L., Varley, N., Gavilanes-Ruiz, J.C., Norini, G., Sarocchi, D., Caballero, L., Cortes,
698 A., 2010. Rainfall-triggered lahars at Volcán de Colima, Mexico: Surface hydro-repellency as
699 initiation process. *J. Volcanol. Geotherm. Res.* 189, 105–117.
700 <https://doi.org/10.1016/j.jvolgeores.2009.10.014>

701 Cascini, L., Cuomo, S., Pastor, M., Sorbino, G., 2010. Modeling of Rainfall-Induced Shallow Landslides
702 of the Flow-Type. *J. Geotech. Geoenvironmental Eng.* 136, 85–98.
703 [https://doi.org/10.1061/\(ASCE\)GT.1943-5606.0000182](https://doi.org/10.1061/(ASCE)GT.1943-5606.0000182)

704 Cascini, L., Cuomo, S., Della Sala, M., 2011. Spatial and temporal occurrence of rainfall-induced
705 shallow landslides of flow type: A case of Sarno-Quindici, Italy. *Geomorphology* 126, 148–158.
706 <https://doi.org/10.1016/j.geomorph.2010.10.038>

707 Castro, J.M., Schipper, C.I., Mueller, S.P., Militzer, A.S., Amigo, A., Parejas, C.S., Jacob, D., 2013.
708 Storage and eruption of near-liquidus rhyolite magma at Cordon Caulle, Chile. *Bull. Volcanol.* 75,
709 1–17. <https://doi.org/10.1007/s00445-013-0702-9>

710 Charbonnier, S.J., Connor, C.B., Connor, L.J., Sheridan, M.F., Oliva Hernández, J.P., Richardson, J.A.,
711 2018. Modeling the October 2005 lahars at Panabaj (Guatemala). *Bull. Volcanol.* 80.
712 <https://doi.org/10.1007/s00445-017-1169-x>

713 Collins, B. D., & Dunne, T., 1986. Erosion of tephra from the 1980 eruption of Mount St. Helens. *Geol.
714 Soc. Am. Bull.* 97, 896–905.

715 CONAE (Comision Navional de Actividades Espaciales) 2011, Argentina. <http://conae.gov.ar/>

716 Córdoba, G., Villarosa, G., Sheridan, M.F., Viramonte, J.G., Beigt, D., Salmuni, G., 2015. Secondary
717 lahar hazard assessment for Villa la Angostura, Argentina, using Two-Phase-Titan modelling code
718 during 2011 Cordón Caulle eruption. *Nat. Hazards Earth Syst. Sci.* 15, 757–766.
719 <https://doi.org/10.5194/nhess-15-757-2015>

720 Crosta, G.B., Dal Negro, P., 2003. Observations and modelling of soil slip-debris flow initiation
721 processes in pyroclastic deposits: the Sarno 1998 event. *Nat. Hazards Earth Syst. Sci.* 3, 53–69.
722 <https://doi.org/10.5194/nhess-3-53-2003>.

723 Cuomo S., & Della Sala, 2016. Spatially distributed analysis of soil erosion in a mountain catchment.
724 In: *Landslides and Engineered Slopes. Experience, Theory and Practice – Aversa et al. (Eds) 2016*
725 *Associazione Geotecnica Italiana, Rome, Italy, ISBN 978-1-138-02988-0, pp: 721 – 728.*

726 Cuomo, S., Iervolino, A., 2016. Investigating the role of stratigraphy in large-area physically-based
727 analysis of December 1999 Cervinara shallow landslides. *Journal of Mountain Science*, 13(1),
728 104-115.

729 Cuomo, S., Della Sala, M., Novità, A., 2015. Physically based modelling of soil erosion induced by
730 rainfall in small mountain basins. *Geomorphology* 243, 106–115.
731 <https://doi.org/10.1016/j.geomorph.2015.04.019>

732 Elissondo, M., Baumann, V., Bonadonna, C., Pistolesi, M., Cioni, R., Bertagnini, A., Biass, S., Herrero,
733 J.C., Gonzalez, R., 2016. Chronology and impact of the 2011 Cordón Caulle eruption, Chile. *Nat.*
734 *Hazards Earth Syst. Sci.* 16, 675–704. <https://doi.org/10.5194/nhess-16-675-2016>

735 Fauqué L., Baumann V. and Gonzalez R., 2011. Comentarios sobre la observación de una avalancha de
736 nieve encauzada en la quebrada Florencia, Villa la Angostura, Neuquén, Servicio Geológico
737 Minero Argentino (SEGEMAR), Buenos Aires, Internal report.

738 Frattini, P., Crosta, G.B., Fusi, N., Dal Negro, P., 2004. Shallow landslides in pyroclastic soils: A
739 distributed modelling approach for hazard assessment. *Eng. Geol.* 73, 277–295.
740 <https://doi.org/10.1016/j.enggeo.2004.01.009>

741 Fredlund, D.G., Xing, A., 1994. Equations for the soil-water characteristic curve. *Can. Geotech. J.* 31,
742 521-532. <https://doi.org/10.1139/t94-120>

743 Gardner, W. R., 1958. Some steady-state solutions of the unsaturated moisture flow equation with
744 application to evaporation from a water table. *Soil science*, 85(4), 228-232.

745 Haddad, B., Pastor, M., Palacios, D., Muñoz-Salinas, E., 2010. A SPH depth integrated model for
746 Popocatepetl 2001 lahar (Mexico): Sensitivity analysis and runout simulation. *Eng. Geol.* 114,
747 312–329. <https://doi.org/10.1016/j.enggeo.2010.05.009>

748 Haneberg, W. C., 1991. Observation and analysis of pore pressure fluctuations in a thin colluvium
749 landslide complex near Cincinnati, Ohio. *Engineering Geology*, 31(2), 159-184.

750 Has, R., Calderón P., S.C. and Molla E., 2012. Evento 22 de enero 2012, reporte a Intendente Cacault.
751 Technical report, Grupo de Rescate de montaña Villa La Angostura, Argentina.

752 Horton, R.E., 1945. Erosional development of streams and their drainage basins; hydrophysical
753 approach to quantitative morphology. *Geological Society of America Bulletin*, 56(3), 275-370.

754 Iverson, R.M., Major, J. J., 1987. Rainfall, ground-water flow, and seasonal movement at Minor Creek
755 landslide, northwestern California: Physical interpretation of empirical relations. *Geological*
756 *Society of America Bulletin*, 99(4), 579-594.

757 Iverson, R.M., Lahusen R.G., 1989. Dynamic Pore-Pressure Fluctuations in Rapidly Shearing Granular
758 Materials. *Am. Assoc. Adv. Sci.* 246, 796–799.

759 Iverson, R. M., 1997. The physics of debris flows. *Reviews of geophysics.* 35, 245-296.

760 Iverson, R.M., Schilling, S.P., Vallance, J.W., 1998. Objective delineation of lahar-inundation hazard
761 zones. *Bull. Geol. Soc. Am.* 110, 972–984. [https://doi.org/10.1130/0016-](https://doi.org/10.1130/0016-7606(1998)110<0972:ODOLIH>2.3.CO;2)
762 [7606\(1998\)110<0972:ODOLIH>2.3.CO;2](https://doi.org/10.1130/0016-7606(1998)110<0972:ODOLIH>2.3.CO;2)

763 Iverson, R.M., 2000. Landslide triggering by rain infiltration. *Water Resour. Res.* 36, 1897–1910.
764 <https://doi.org/10.1029/2000WR900090>

765 Janda, R., Daag, A., Delos Reyes, P., Newhall, C., Pierson, T., Punongbayan, R., Rodolfo, K., 1996.
766 Assessment and Response to Lahar Hazard around Mount Pinatubo, 1991 to 1993. *Fire Mud;*
767 *Eruptions Lahars Mt. Pinatubo, Philipp.* 107–139.

768 Kubanek, J., Richardson, J.A., Charbonnier, S.J., Connor, L.J., 2015. Lava flow mapping and volume
769 calculations for the 2012–2013 Tolbachik, Kamchatka, fissure eruption using bistatic TanDEM-X
770 InSAR. *Bull. Volcanol.* 77, 1–13. <https://doi.org/10.1007/s00445-015-0989-9>

771 Lavigne, F., Thouret, J.-C., Voight, B., Young, K., LaHusen, R., Marso, J., Suwa, H., Sumaryono, A.,
772 Sayudi, D., Dejean, M., 2000a. Instrumental lahar monitoring at Merapi Volcano, Central Java,
773 Indonesia. *J. Volcanol. Geotherm. Res.* 100, 457–478. [https://doi.org/10.1016/S0377-](https://doi.org/10.1016/S0377-0273(00)00151-7)
774 [0273\(00\)00151-7](https://doi.org/10.1016/S0377-0273(00)00151-7)

775 Lavigne, F., Thouret, J., Voight, B., Suwa, H., Sumaryono, A., 2000b. Lahars at Merapi volcano,
776 Central Java: an overview. *J. Volcanol. Geotherm. Res.* 100, 423–456.
777 [https://doi.org/10.1016/S0377-0273\(00\)00150-5](https://doi.org/10.1016/S0377-0273(00)00150-5)

778 Lavigne, F., Suwa, H., 2004. Contrasts between debris flows, hyperconcentrated flows and stream flows
779 at a channel of Mount Semeru, East Java, Indonesia. *Geomorphology* 61, 41–58.
780 <https://doi.org/10.1016/j.geomorph.2003.11.005>

781 Leavesley, G. H., Lusby, G. C., Lichty, R. W., 1989. Infiltration and erosion characteristics of selected
782 tephra deposits from the 1980 eruption of Mount St. Helens, Washington, USA. *Hydrological*
783 *sciences journal*, 34(3), 339-353.

784 Levandowsky, M., Winter D., 1971. Distance between sets. *Nature* 234, 174.
785 <https://doi.org/10.1038/239174c0>

786 Major, J.J., Pierson, T.C., Dinehart, R.L., Costa, J.E., 2000. Sediment yield following severe volcanic
787 disturbance - A two-decade perspective from Mount St. Helens. *Geology* 28, 819–822.
788 [https://doi.org/10.1130/0091-7613\(2000\)28<819:SYFSVD>2.0.CO;2](https://doi.org/10.1130/0091-7613(2000)28<819:SYFSVD>2.0.CO;2)

789 Major, J.J., Yamakoshi, T., 2005. Decadal-scale change of infiltration characteristics of a tephra-mantled
790 hillslope at Mount St Helens, Washington. *Hydrol. Process.* 19, 3621–3630.
791 <https://doi.org/10.1002/hyp.5863>

792 Manville, V., White, J. D. L., Hodgson, K. A., 2000. Dynamic interactions between lahars and stream
793 flow: A case study from Ruapehu volcano, New Zealand: Discussion and reply:
794 Discussion. *Geological Society of America Bulletin*, 112(7), 1149-1151.

795 Manville, V., Németh, K., Kano, K., 2009. Source to sink: A review of three decades of progress in the
796 understanding of volcanoclastic processes, deposits, and hazards. *Sediment. Geol.* 220, 136–161.
797 <https://doi.org/10.1016/j.sedgeo.2009.04.022>

798 Manville, V., Major, J. J., Fagents, S. A., 2013. Modeling lahar behaviour and hazards. In: S.A. Fagents,
799 T.K.P. Gregg, R.M.C. Lopes (Eds), *Modeling volcanic processes: the physics and mathematics of*
800 *volcanism*, Cambridge University Press, 300-330.

801 Martínez Pastur, G., Lencinas, M.V., Peri, P.L., Arena, M., 2007. Photosynthetic plasticity of
802 *Nothofagus pumilio* seedlings to light intensity and soil moisture. *For. Ecol. Manage.* 243, 274–
803 282. <https://doi.org/10.1016/j.foreco.2007.03.034>

804 Mead, S., Magill, C., Hilton, J., 2016. Rain-triggered lahar susceptibility using a shallow landslide and
805 surface erosion model. *Geomorphology* 273, 168–177.
806 <https://doi.org/10.1016/j.geomorph.2016.08.022>

807 Montgomery, D.R., Dietrich, W.E., 1994. A physically based model for the topographic control on
808 shallow landsliding. *Water Resour. Res.* 30, 1153–1171. <https://doi.org/10.1029/93WR02979>

809 Montgomery, D.R., Sullivan, K., Greenberg, H.M., 1998. Regional test of a model for shallow
810 landsliding. *Hydrol. Process.* 12, 943–955. [https://doi.org/10.1002/\(SICI\)1099-1085\(199805\)12:6<943::AID-HYP664>3.0.CO;2-Z](https://doi.org/10.1002/(SICI)1099-1085(199805)12:6<943::AID-HYP664>3.0.CO;2-Z)

811

812 Naranjo, J.A., Singer, B.S., Jicha, B.R., Moreno, H., Lara, L.E., 2017. Holocene tephra succession of
813 Puyehue-Cordón Caulle and Antillanca/Casablanca volcanic complexes, southern Andes (40–
814 41°S). *J. Volcanol. Geotherm. Res.* 332, 109–128.
815 <https://doi.org/10.1016/j.jvolgeores.2016.11.017>

816 O’Brian J.S., Julian P.Y. and Fullerton W.T., 1993. Two-dimensional Water flood and mud flow
817 simulation. *Hydraulic Eng. ASCE* 119 (2): 244-261.

818 O’loughlin, E. M., 1986. Prediction of surface saturation zones in natural catchments by topographic
819 analysis. *Water Resources Research*, 22(5), 794-804. doi:[10.1029/WR022i005p00794](https://doi.org/10.1029/WR022i005p00794)

820 Philip, J. R., 1991, Hillslope infiltration: Planar slopes, *Water Resour. Res.*, 27(1), 109–117,
821 doi:[10.1029/90WR01704](https://doi.org/10.1029/90WR01704).

822 Pierson, T.C., Janda, R.J., Thouret, J.-C., Borrero, C.A., 1990. Perturbation and melting of snow and ice
823 by the 13 November 1985 eruption of Nevado del Ruiz, Colombia, and consequent mobilization,
824 flow and deposition of lahars. *J. Volcanol. Geotherm. Res.* 41, 17–66.
825 [https://doi.org/10.1016/0377-0273\(90\)90082-Q](https://doi.org/10.1016/0377-0273(90)90082-Q)

826 Pierson, T.C., Janda, R.J., Umbal, J. V, Daag, a S., 1992. Immediate and long-term hazards from lahars
827 and excess sedimentation in rivers draining Mount Pinatubo, Philippines. U.S. Geol. Surv. Water-
828 Resour. Invest. Rep pp, 92–403937

829 Pierson T.C., 2005. Hyperconcentrated flow — transitional process between water flow and debris flow.
830 In: Debris-flow Hazards and Related Phenomena. Springer Praxis Books. Springer, Berlin,
831 Heidelberg. https://doi.org/10.1007/3-540-27129-5_8

832 Pierson, T.C., Major, J.J., Amigo, Á., Moreno, H., 2013. Acute sedimentation response to rainfall
833 following the explosive phase of the 2008-2009 eruption of Chaitén volcano, Chile. *Bull. Volcanol.*
834 75, 1–17. <https://doi.org/10.1007/s00445-013-0723-4>

835 Pierson, T.C., Major, J.J., 2014. Hydrogeomorphic Effects of Explosive Volcanic Eruptions on Drainage
836 Basins. *Annu. Rev. Earth Planet. Sci.* 42, 469–507. [https://doi.org/10.1146/annurev-earth-060313-](https://doi.org/10.1146/annurev-earth-060313-054913)
837 054913

838 Pistolesi, M., Cioni, R., Bonadonna, C., Elissondo, M., Baumann, V., Bertagnini, A., Chiari, L.,
839 Gonzales, R., Rosi, M., Francalanci, L., 2015. Complex dynamics of small-moderate volcanic
840 events: the example of the 2011 rhyolitic Cordón Caulle eruption, Chile. *Bull. Volcanol.* 77.
841 <https://doi.org/10.1007/s00445-014-0898-3>

842 Reid, M. E., 1994. A pore-pressure diffusion model for estimating landslide-inducing rainfall. *The*
843 *Journal of Geology*, 102(6), 709-717.

844 Rossi, G., Catani, F., Leoni, L., Segoni, S., & Tofani, V., 2013. HIRESSS: a physically based slope
845 stability simulator for HPC applications. *Natural Hazards and Earth System Sciences*, 13(1), 151.

846 Savage, W. Z., Godt, J. W., Baum, R. L., 2003. A model for spatially and temporally distributed shallow
847 landslide initiation by rainfall infiltration. In: 3rd International Conference on Debris-Flow Hazards
848 Mitigation: Mechanics, Prediction, and Assessment, Vol. 1, pp. 179-187.

849 Savage, W. Z., Godt, J. W., Baum, R. L., 2004. Modeling time-dependent areal slope
850 stability. *Landslides: evaluation and stabilization*. Balkema, Taylor & Francis Group, London, 23-
851 38.

852 Scott, W.E., Hoblitt, R.P., Torres, R.C., Self, S., Martinez, M.L., Nillos, T., 1996. Pyroclastic flows of
853 the June 15, 1991, climactic eruption of Mount Pinatubo. *Fire Mud eruptions lahars Mt. Pinatubo.*
854 *Philipp.* 545–570.

855 Scott, K.M., Vallance, J.W., Kerle, N., Macías, J.L., Strauch, W., Devoli, G., 2005. Catastrophic
856 precipitation-triggered lahar at Casita volcano, Nicaragua: Occurrence, bulking and
857 transformation. *Earth Surf. Process. Landforms* 30, 59–79. <https://doi.org/10.1002/esp.1127>

858 Sheridan, M.F., Stinton, A.J., Patra, A., Pitman, E.B., Bauer, A., Nichita, C.C., 2005. Evaluating
859 Titan2D mass-flow model using the 1963 Little Tahoma Peak avalanches, Mount Rainier,
860 Washington. *J. Volcanol. Geotherm. Res.* 139, 89–102.
861 <https://doi.org/10.1016/j.jvolgeores.2004.06.011>

862 Singer, B.S., Jicha, B.R., Harper, M.A., Naranjo, J.A., Lara, L.E., Moreno-Roa, H., 2008. Eruptive

863 history, geochronology, and magmatic evolution of the Puyehue-Cordón Caulle volcanic complex,
864 Chile. *Bull. Geol. Soc. Am.* 120, 599–618. <https://doi.org/10.1130/B26276.1>

865 Smith, G. A., 1986. Coarse-grained nonmarine volcanoclastic sediment: Terminology and depositional
866 process. *Geological Society of America Bulletin*, 97(1), 1-10.

867 Smith, G. A., & Lowe, D. R., 1991. Lahars: Volcano Hydrologic-Events and Deposition in the Debris
868 Flow—Hyperconcentrated Flow Continuum. *Sedimentation in Volcanic Settings*, SEPM (Society
869 for Sedimentary Geology) Special Publication N° 45.

870 Sorbino, G., Sica, C., Cascini, L., & Cuomo, S., 2007. On the forecasting of flowslides triggering areas
871 using physically based models. In *Proceedings of 1st North American landslides conference AEG*
872 *Special Publication*, Vol. 1, pp. 305-315.

873 Sorbino, G., Sica, C., Cascini, L., 2010. Susceptibility analysis of shallow landslides source areas using
874 physically based models. *Nat. Hazards* 53, 313–332. <https://doi.org/10.1007/s11069-009-9431-y>

875 Srivastava, R., & Yeh, T. C. J., 1991. Analytical solutions for one-dimensional, transient infiltration
876 toward the water table in homogeneous and layered soils. *Water Resources Research*, 27(5), 753-
877 762.

878 Taborton, D.G. 1997. A new method for the determination of flow direction and upslope area in grid
879 digital elevation models. *Water Resource Research*, 33(2), pp.309-319. Doi:10.129/96wr03137

880 Tarolli, P., Tarboton, D.G., 2006. A new method for determination of most likely landslide initiation
881 points and the evaluation of digital terrain model scale in terrain stability mapping. *Hydrol. Earth*
882 *Syst. Sci.* 10, 663–677. <https://doi.org/10.5194/hess-10-663-2006>

883 Vallance, J. W., 2000. Lahars. *Encyclopedia of volcanoes*, 601-616.

884 Van Westen, C.J., Daag, A.S., 2005. Analysing the relation between rainfall characteristics and lahar
885 activity at Mount Pinatubo, Philippines. *Earth Surf. Process. Landforms* 30, 1663–1674.
886 <https://doi.org/10.1002/esp.1225>

887 Volentik, A.C.M., Connor, C.B., Connor, L.J., Bonadonna, C., 2009. Aspects of volcanic hazard
888 assessment for the Bataan nuclear power plant, Luzon Peninsula, Philippines. *Volcan. Tecton.*
889 *Hazard Assess. Nucl. Facil.* 9780521887, 229–256.
890 <https://doi.org/10.1017/CBO9780511635380.010>

891 Worni, R., Huggel, C., Stoffel, M., Pulgarín, B., 2012. Challenges of modeling current very large lahars
892 at Nevado del Huila Volcano, Colombia. *Bull. Volcanol.* 74, 309–324.
893 <https://doi.org/10.1007/s00445-011-0522-8>

894 Yamakoshi, T., Suwa, H., 2000. Post-eruption characteristics of surface runoff and sediment discharge
895 on the slopes of pyroclastic-flow deposits, Mount Unzen, Japan. *Chikei* 21, 469–497.

896 Yamamoto, H., 1984. Erosion of the 1977–1978 tephra layers on a slope of Usu Volcano,
897 Hokkaido. *EOS, Transactions, American Geophysical Union*, 5(2), 111-124.

898 Zanchetta, G., Sulpizio, R., Pareschi, M.T., Leoni, F.M., Santacroce, R., 2004. Characteristics of May
899 5-6, 1998 volcanoclastic debris flows in the Sarno area (Campania, southern Italy): Relationships

900 to structural damage and hazard zonation. J. Volcanol. Geotherm. Res. 133, 377–393.
901 [https://doi.org/10.1016/S0377-0273\(03\)00409-8](https://doi.org/10.1016/S0377-0273(03)00409-8)
902

903 **Figure captions**

904 Figure 1: A) Isopach map on shaded relief of the cumulative Cordón Caulle 2011 tephra fall deposit in
905 the proximal and medial area, after Pistolesi et al. (2015). Isolines between 0.2 and 3 cm from Gaitan et
906 al. (2011). Black dots represent the tephra outcrops measured in 2012 and 2013 field campaign (Pistolesi
907 et al., 2015). The red square indicates the study area between the Argentina-Chile border and Villa La
908 Angostura. B) Map of study area along the Road n. 231. The green hexagons indicate the 2016 sample
909 locations. The blue squares are the meteorological stations: M1, Paráje Rincon; and M2, Villa La
910 Angostura. The red triangles represent the locations of observations of 2011 and 2012 lahar deposits:
911 L1, Diana waterfalls; L2, 231 road; and L3, Maderera Misiones. The light brown line delimitates the
912 watershed of Villa la Angostura.

913

914 Figure 2: A) Tephra sequence on April 2012 in the town of Villa La Angostura. Unit I = 4 cm; Unit II
915 = 3cm; Unit III = 5,5 cm. B) Tephra sequence on December 2016 located in Cerro Bayo (fig 1, S3), in
916 a small Nothofagus forest at 1530 m, with a slope inclination of 35 ° (Fig.1b, S3). Unit I = 4 cm; Unit
917 II = 1cm; Unit III = 6 cm; and remobilized tephra on the top.

918

919 Figure 3: Timeline between June 2011 and June 2012 showing the daily rainfall data measured at A)
920 Rincón rain gauge, near Chile- Argentina border, and B) Villa La Angostura. Occurrences of lahar and
921 flood events during this time are marked.

922

923 Figure 4: A) Photograph of a big ditch formed through road N. 231 during the 10 June 2011 lahar event
924 near the Chile-Argentina border (photo Diario de Villa La Angostura,
925 <https://www.diarioandino.com.ar/>). B) Lahar deposit at the foot of the “Diana” waterfall, located 100m
926 upstream from road N. 231. C) Photograph of the 2 June 2012 flood event which damaged a house on
927 the Totoral River alluvial plain (photo Diario de Villa La Angostura <https://www.diarioandino.com.ar/>)
928 D) Photograph of the Totoral River and terrace with dead trees and flooding volcanic sediment deposit.
929 The red line indicates the flood deposit.

930 Figure 5: 1) Photograph of the 10 June lahar deposit, 100 m upstream from road N. 231 (L2 in Fig. 1b).
931 The stratigraphic section represents 5 beds of alternating type A and type B lithofacies. 2) Photograph
932 of an exposure of lahar deposit in “Diana waterfalls” creek (L2 in Fig 1b). The stratigraphic section
933 shows a sequence of 7 beds with 3 different types of lithofacies (C, D and E).

934 Figure 6: Sketch of tephra sequence and thicknesses for scenarios 1 and 2.

935

936 Figure 7: Plot of the percentage of unstable area against a range of cohesion from 0 to 1.5 kPa. Calculated
937 with TRIGRS for scenario 1 and Colorado River upper catchment

938

939 Figure 8: Sketch illustrating the relationship between True positive (TR), False positive (FP), False
940 negative and True negative. Simulated unstable area: A_{sim} ; observed source area: A_{obs} .

941 Figure 9A) Geomorphological map of six catchments in Villa la Angostura. River and catchment names:
942 I-Las Piedritas, II-Colorado, III-Florencia, IV-La Ponderosa, V-Maderera Misiones, VI-El Muerto. B)
943 Florencia river upper catchment on November 2011. On the left-side, rills formed just below the hillside
944 crest, transporting tephra and rock boulder. On the right-side, tephra is removed by shallow landslides
945 on the steep hillslope. C) Remobilized tephra deposit in a first order channel depression, located in the
946 upper Colorado catchment.

947

948 Figure 10: Schematic evolution of tephra erosion between June 2011 and December 2016 in the
949 Florencia River upper catchment. Arrows in figures A, B and C indicate the location of the photographs.

950

951 Figure 11: Instability maps obtained with SHALSTAB for scenario 1 with a critical rainfall of 5 mm/day
952 and A) no cohesion and B) cohesion included. Different colours correspond to ranges of $\log(q/T)$ (Un.
953 (un)stable: Unconditionally (un)stable).

954

955 Figure 12: Time evolution of the percentage of unstable areas in the Colorado upper watershed
956 calculated with TRIGRS for scenario 1, with layer thicknesses of a) 0.15 m and b) 0.2 m, and scenario
957 2 with thicknesses of c) 0.1 m and d) 0.2 m. Simulations were performed with 3 different rainfall
958 intensities and durations (3.3 mm/h, 24h; 1.6 mm/h, 48h; 0.83 mm/h, 72h).

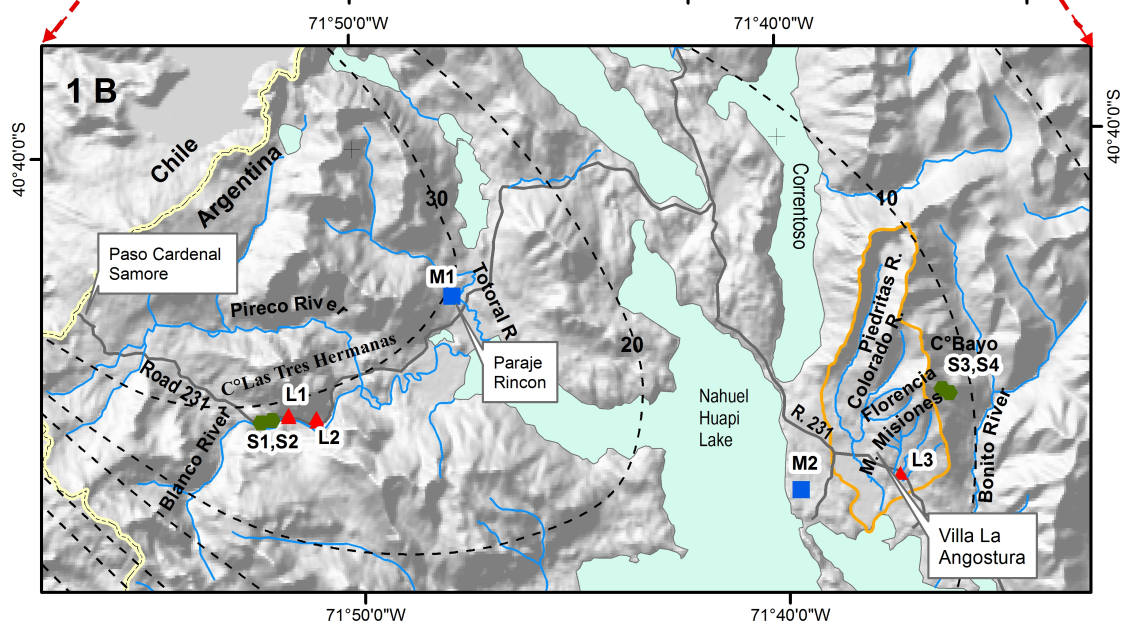
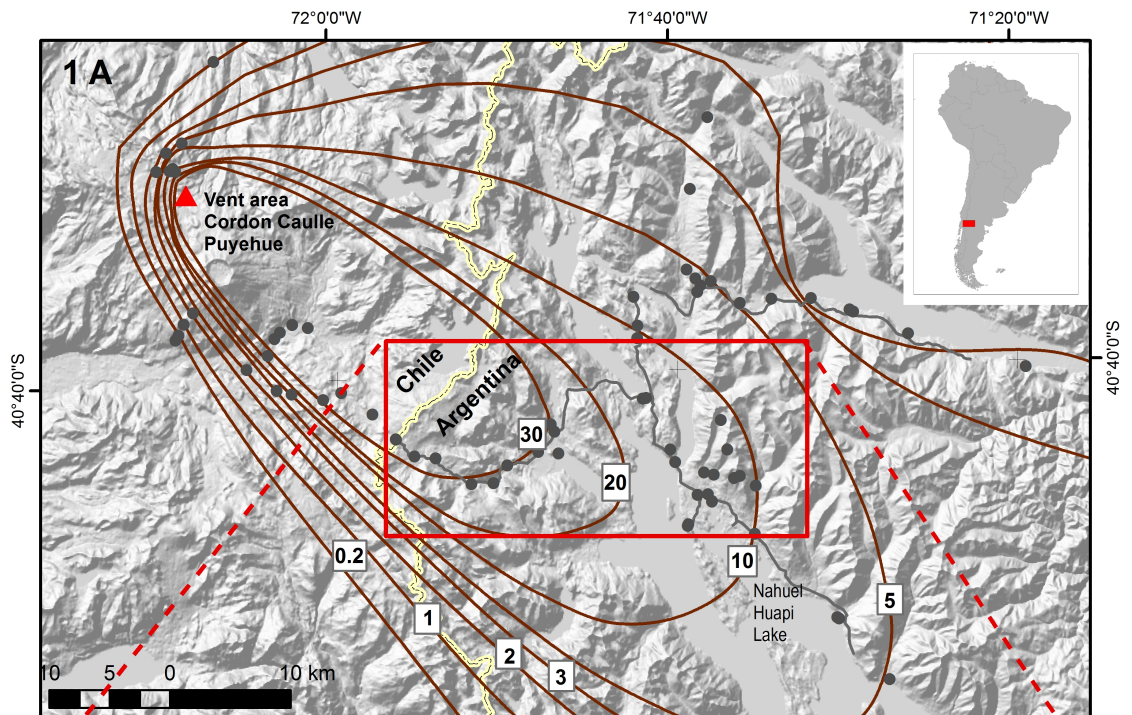
959

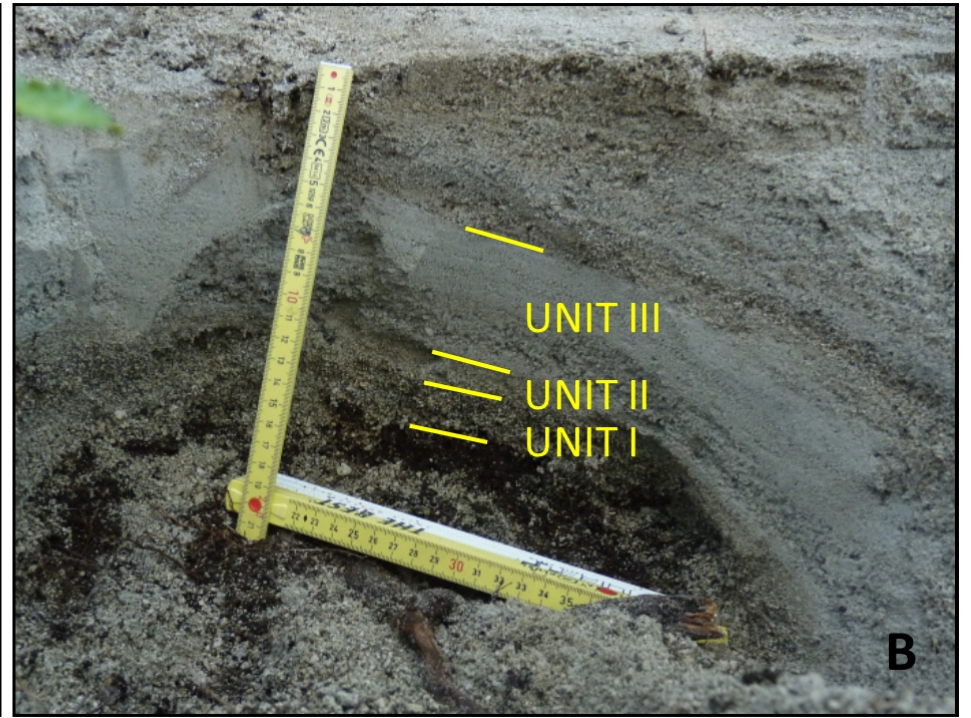
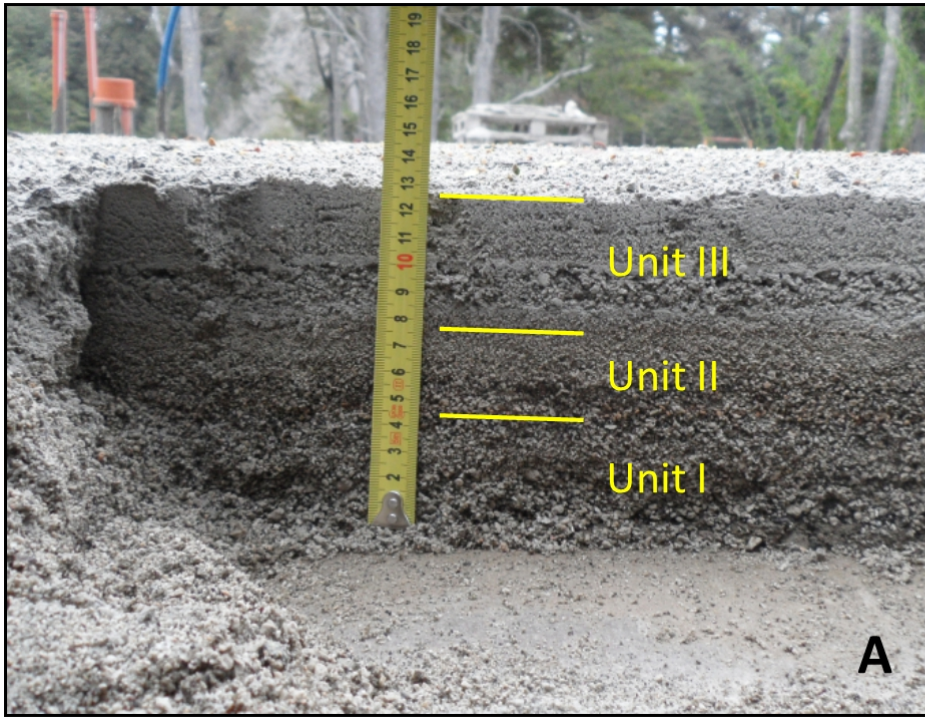
960 Figure 13: Time evolution of the percentage of unstable areas in the Florencia Rivers upper watershed
961 calculated with TRIGRS for scenario 1, with layer thicknesses of a) 0.15 m and b) 0.2 m, and scenario
962 2 with thicknesses of c) 0.1 m and d) 0.2 m. Simulations were performed with 3 different rainfall
963 intensities and durations (3.3 mm/h, 24h; 1.6 mm/h, 48h; 0.83 mm/h, 72h).

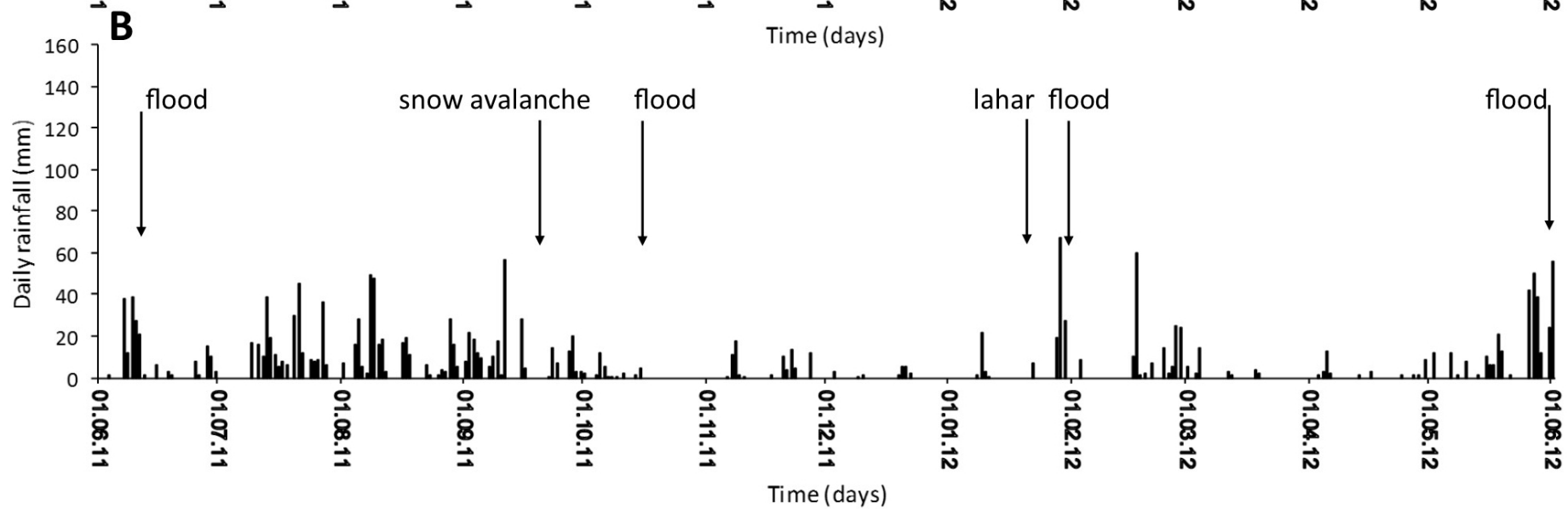
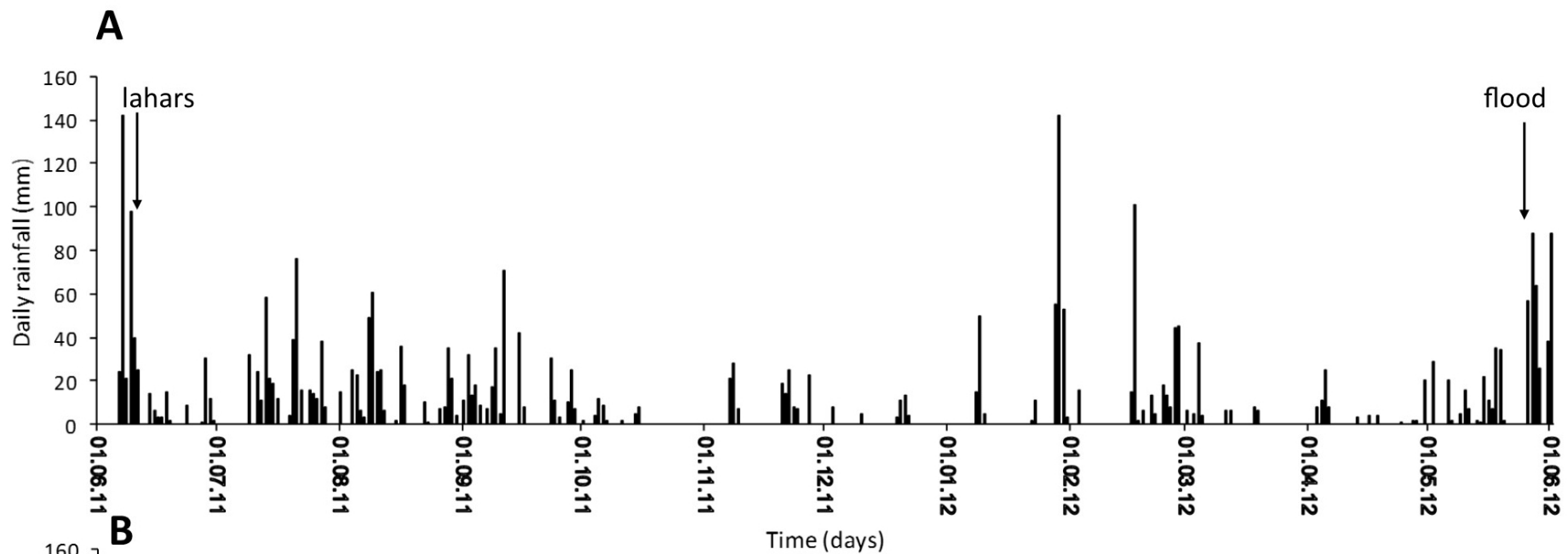
964

965 Figure 14: A) Map of observed lahar source areas in Florencia upper catchment. B, C) Instability maps,
966 obtained with TRIGRS, for B) scenario 1 and C) scenario 2, with a constant rainfall flux of 3.3 mm/h
967 for 24 hours The black line in B) and c) separates forested area on the lower side from bare soil area on
968 the upper side.

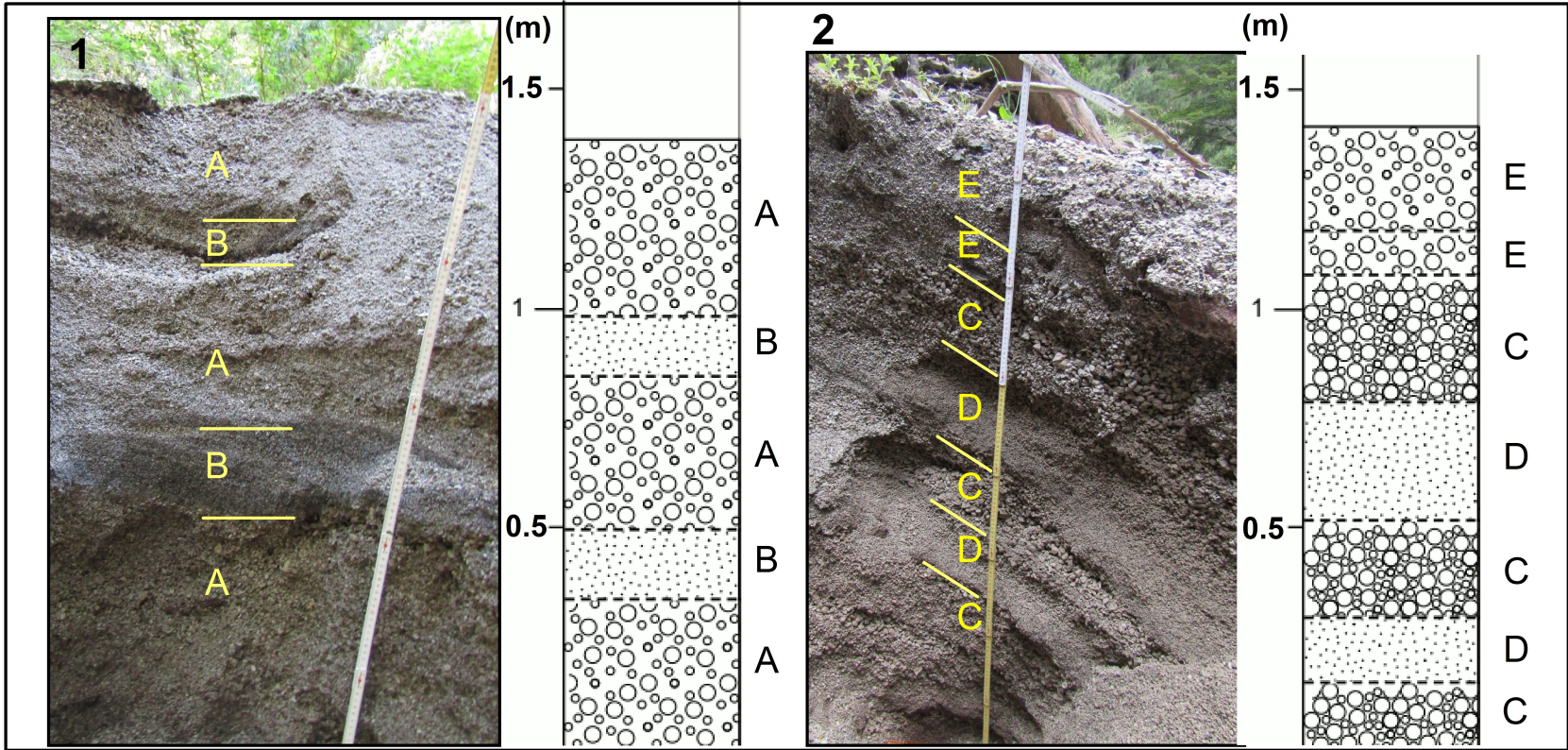
969





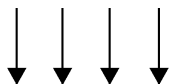






S1

Rainfall



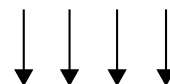
Ash
Lapilli



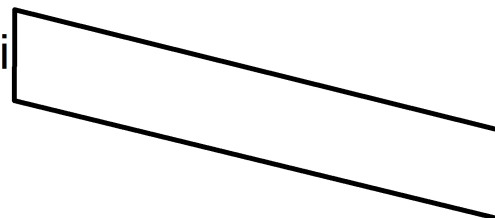
15 cm
(30 cm)

S2

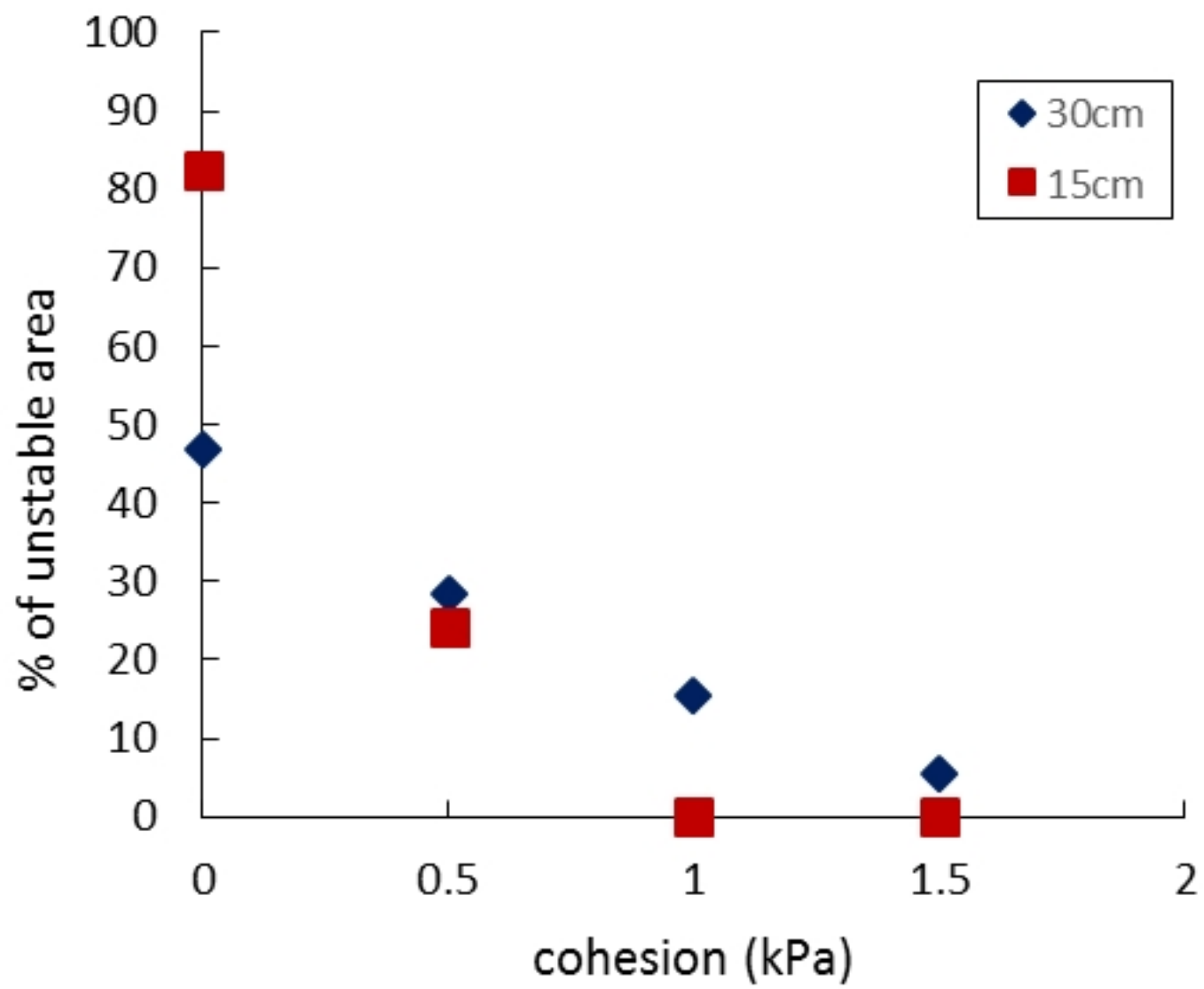
Rainfall

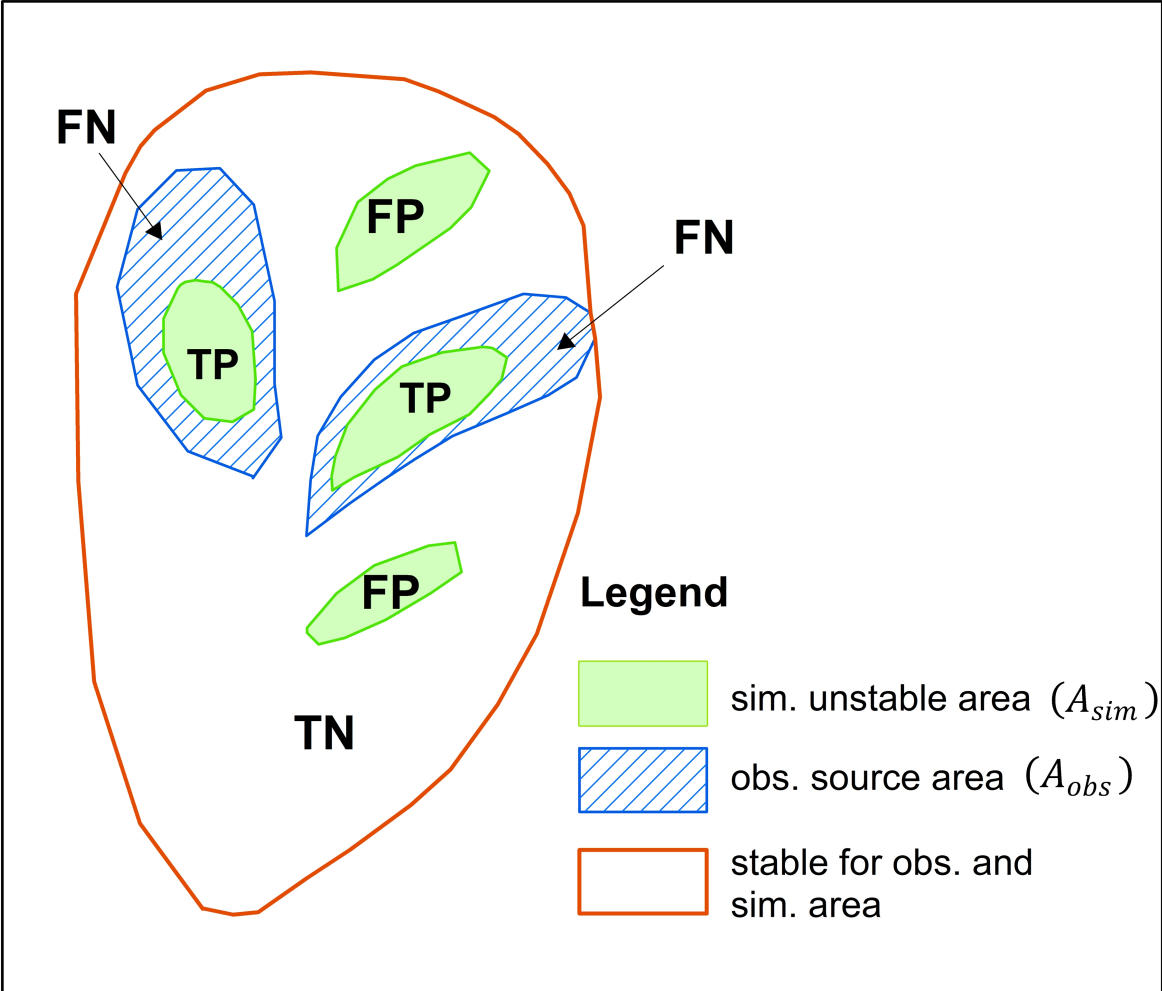


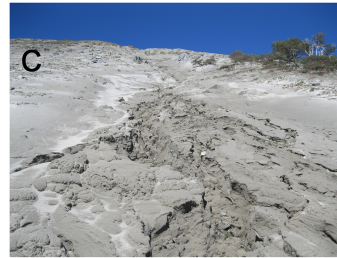
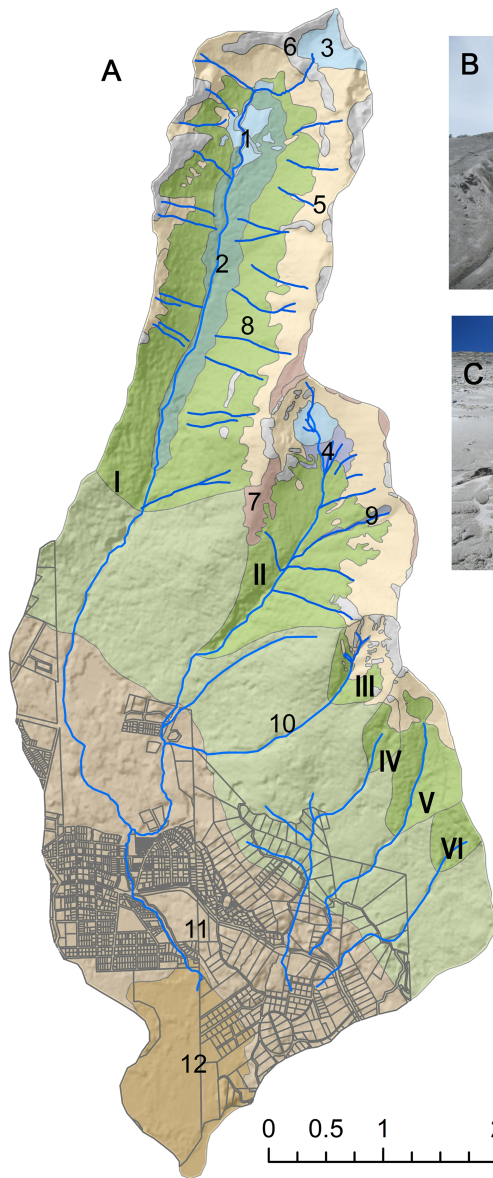
Lapilli



10 cm
(20 cm)


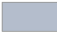





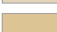
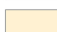
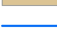
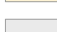

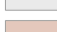
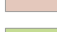


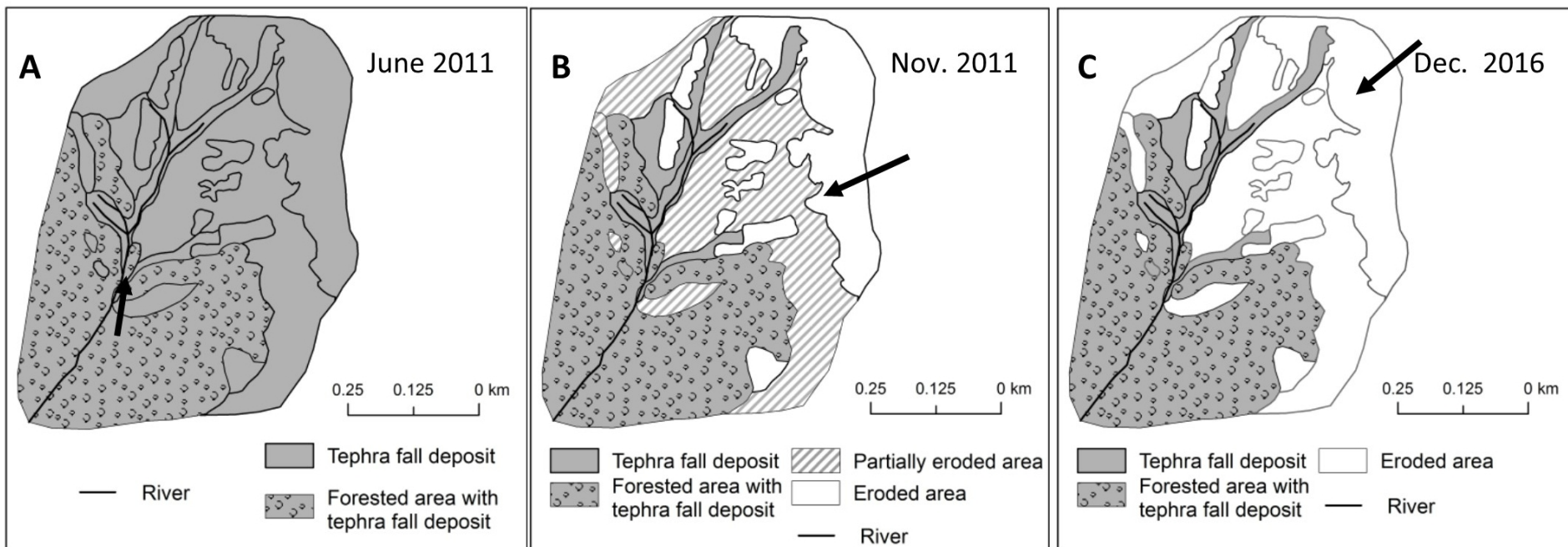


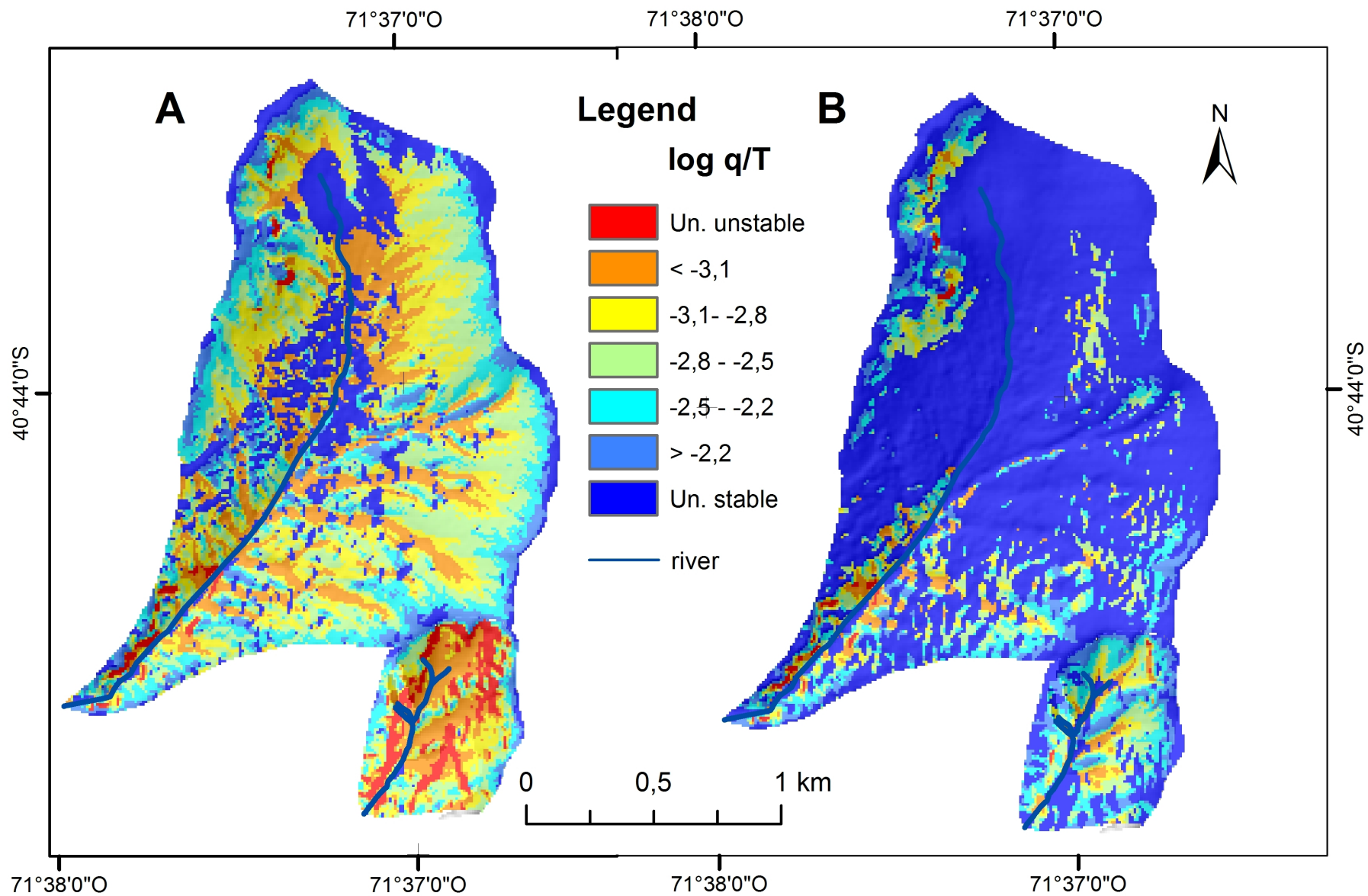


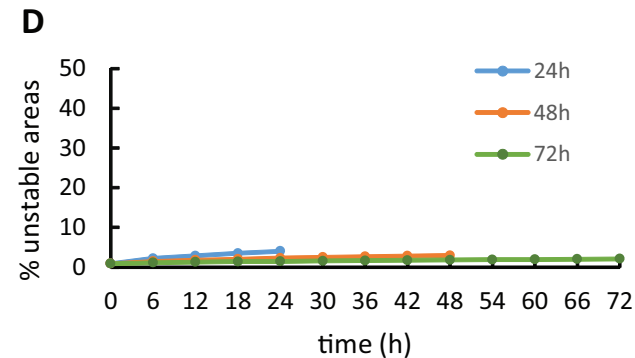
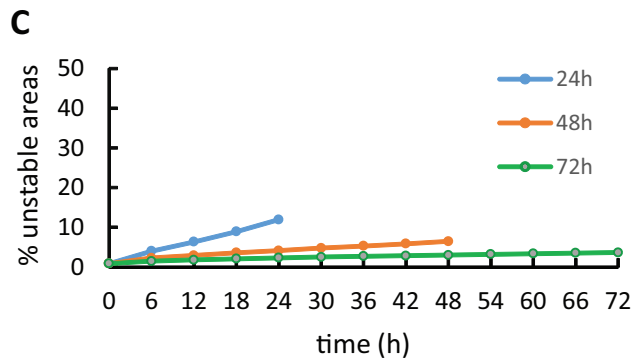
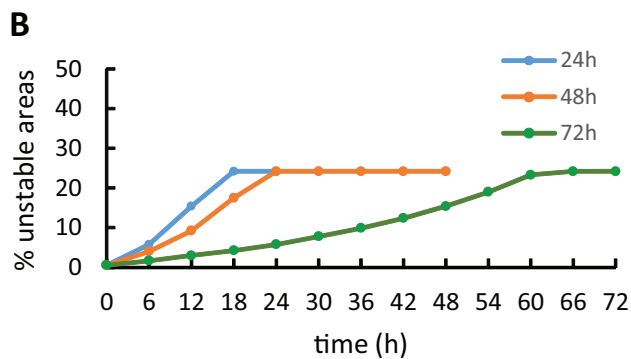
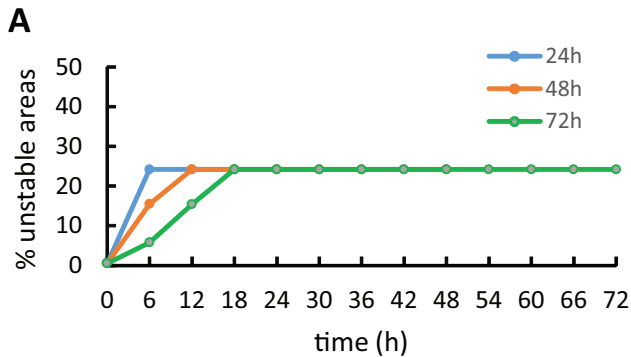
0 0.5 1 2 Kilometers

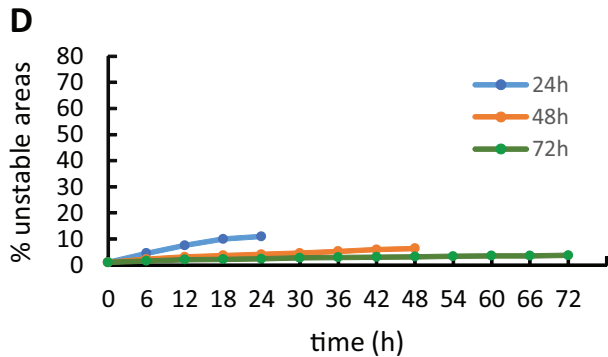
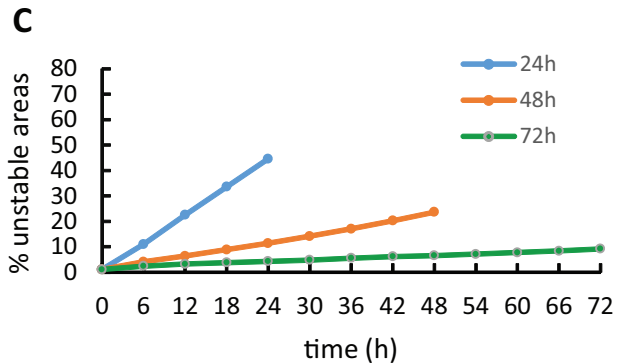
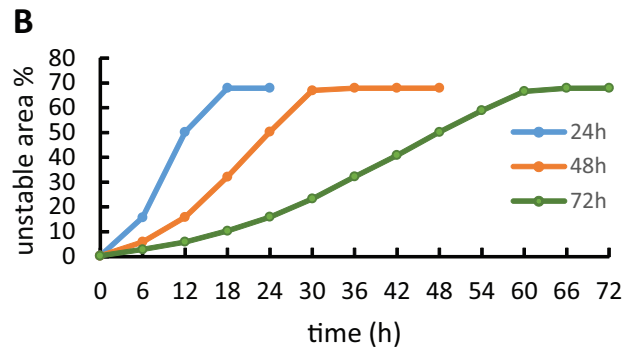
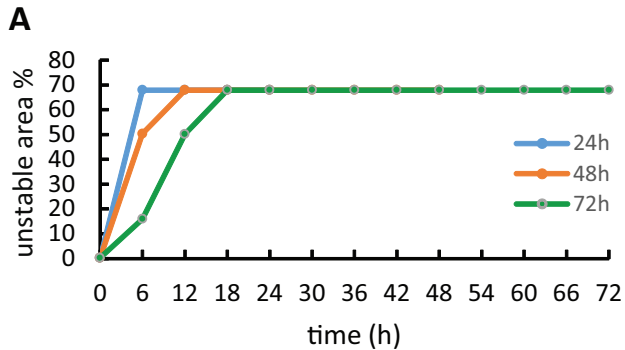
Geomorphological units

- | | |
|---|--|
|  1, Alluvial plain |  9, Debris flow channel |
|  2, Forested alluvial plain |  10, Regional valley flank slope |
|  3, Old glacial cirque depression |  11, Proximal alluvial fan |
|  4, Old cirque front slope |  12, Distal alluvial fan |
|  5, Talus debris slope |  River |
|  6, Rock outcrop |  Villa la Angostura Plots of land |
|  7, Glacially smoothed valley interfluvies | I-VI Upper catchments and River |
|  8, Forested hillslope | |









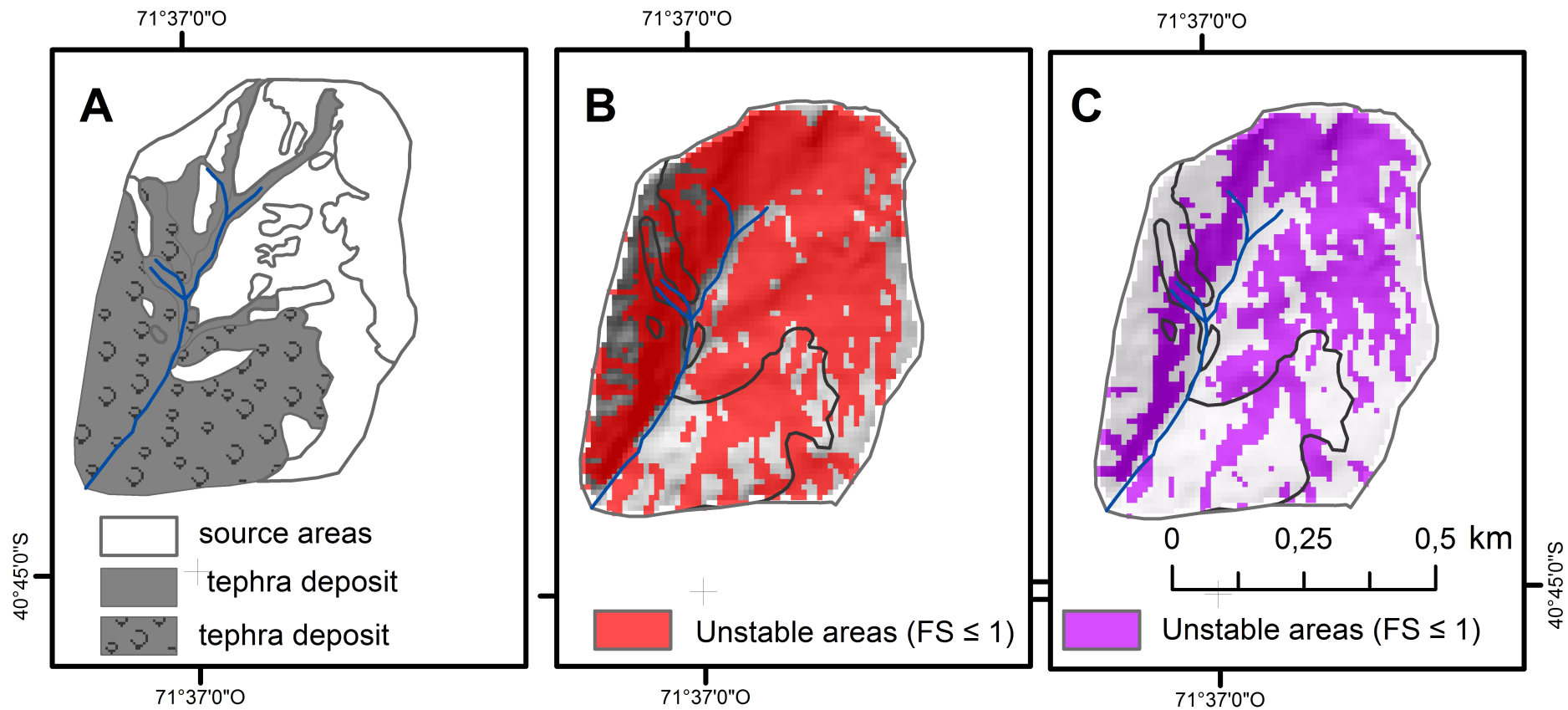


Table 1: Input parameters for SHALSTAB and TRIGRS (scenario 1: ash layer, unit III). **Z**: tephra fallout deposit thickness. K_{sat} was taken from literature. D_0 was computed referring to the procedure reported by Rossi et al. (2013). $T = K_{sat} * Z$. ϕ' and c' were obtained from standard direct shear tests in the geotechnical laboratory of University of Salerno. γ_{sat} was investigated in the laboratory. α , θ_r and θ_s were estimated through analytical procedure.

| Z | Ks | Do (1) | T | ϕ' | γ_s | c' | θ_s | θ_r | α |
|----------|----------------------|----------------------|------------------------|---------------------------|------------------------------|------------------------|------------------------------|------------------------------|----------------------------|
| (m) | (m/s) | (m ² /s) | (m ² /s) | (deg) | kN/m ³ | (kPa) | ths | thr | alp |
| 0.15 | 5 x 10 ⁻⁵ | 5 x 10 ⁻⁵ | 7.5 x 10 ⁻⁶ | 38.4 | 15.6 | 0.5 | 0.62 | 0.06 | 0.08 |

Table 2: Input parameters for SHALSTAB and TRIGRS (scenario 2: lapilli layer, units I and II) K_{sat} was measured in the field. D_0 was computed referring to the procedure reported by Rossi et al. (2013). T , ϕ' and c' were obtained from standard direct shear tests in the geotechnical laboratory of University of Salerno. γ_{sat} was investigated in the laboratory.

| Z | Ks | Do (1) | T | ϕ' | γ_s | c' |
|----------|------------------------|------------------------|------------------------|---------------------------|------------------------------|------------------------|
| (m) | (m/s) | (m ² /s) | (m ² /s) | (deg) | kN/m ³ | (kPa) |
| 0.1 | 3.9 x 10 ⁻² | 1.8 x 10 ⁻² | 5.8 x 10 ⁻³ | 53 | 13 | 0 |

Table 3: Rainfall intensities and duration used in TRIGRS simulations. We assumed that a constant rainfall flux of 3.3 mm/h for 24 hours represent a high intensity rainfall. As well, a medium intensity of 1.6 mm/h and a low intensity of 0.83 mm/day were considered for 48 hours and 72 hours, respectively. For forested area we considered a rainfall interception of 25% and calculated the intensities according to this.

| Duration | Rainfall intensity | |
|----------|--------------------|----------|
| | bare soil | forested |
| h | mm/h | mm/h |
| 24 | 3.30 | 2.50 |
| 48 | 1.60 | 1.25 |
| 72 | 0.83 | 0.63 |

Table 4: Percent of catchment area in each critical rainfall range for scenario 1 with SHALSTAB for the upper catchments Colorado and Florencia River

| basin | | | | Colorado | Florencia | Colorado | Florencia |
|--------------|-----------|-----------------------|----------|----------|-----------|----------|-----------|
| cohesion | | | | 0kPa | 0kPa | 0.5kPa | 0.5kPa |
| class | log (q/T) | T | q | area | area | area | area |
| | | (m ² /day) | (mm/day) | % | % | % | % |
| Un. unstable | -10 | 0.648 | 0.3 | 7.3 | 21.6 | 0.5 | 0.3 |
| unstable | <-3.1 | 0.648 | 0.5 | 24.8 | 28.7 | 2.3 | 6.1 |
| unstable | -2.8 | 0.648 | 1.0 | 19.6 | 14.9 | 3.2 | 8.4 |
| unstable | -2.5 | 0.648 | 2.0 | 17.4 | 16.1 | 6.9 | 16.8 |
| unstable | -2.2 | 0.648 | 4.1 | 8.7 | 10.3 | 6.5 | 21.3 |
| stable | >1.9 | 0.648 | 8.2 | 4.3 | 5.7 | 4.6 | 14.4 |
| Un. Stable | 10 | 0.648 | | 18.0 | 2.9 | 76.0 | 32.6 |

T: Transmissivity; q: critical rainfall; Un.: unconditionally

Table 5: Summary of unstable percentage area for Colorado River and Florencia River upper catchment calculated with TRIGRS model for scenario 1 and 2, for 3 rainfall intensities and duration (3.3, 24h; 1.6, 48h; 0.83 mm/h, 72h) and two different tephra deposit thicknesses for each scenario.

| model | percentage of unstable area | | | |
|---------|-----------------------------|-----------|-----------|----------|
| TRIGRS | C (15cm) | F (15cm) | C (30 cm) | F (30cm) |
| S1, 24h | 24.2% | 68.0% | 24.2% | 68.0% |
| S1, 48h | 24.2% | 68.0% | 24.2% | 68.0% |
| S1, 72h | 24.2% | 68.0% | 24.2% | 68.0% |
| TRIGRS | C (10cm) | F (10 cm) | C (20cm) | F (20cm) |
| S2, 24h | 11.9% | 44.6% | 4.0% | 11.0% |
| S2, 48h | 6.5% | 23.6% | 2.9% | 6.3% |
| S2, 72h | 3.6% | 9.2% | 2.1% | 3.7% |

C: Colorado River upper catchment; F: Florencia River upper catchment; (15 cm): tephra deposit thickness; S1: scenario 1; s2: scenario 2.

Table 6: Performance evaluation for results from two scenario and three rainfall intensity and duration for TRIGRS model and one scenario with and without cohesion for SHALSTAB model, based on Jaccard fit, model precision and model sensitivity.

| Model and scenario | Validation metrics | | Bayesian metrics | |
|--------------------|-----------------------|------------------------|--------------------------|--|
| | Jaccard fit (R_j) | Precision (R_{MP}) | Sensitivity (R_{MS}) | |
| TRIGRS S1, 24h | 47.1% | 56.9% | 73.2% | |
| TRIGRS S1, 48h | 47.1% | 56.9% | 73.2% | |
| TRIGRS S1, 72h | 47.1% | 56.9% | 73.2% | |
| TRIGRS S2, 24h | 40.5% | 62.9% | 53.1% | |
| TRIGRS S2, 48h | 23.4% | 61.3% | 27.4% | |
| TRIGRS S2, 72h | 9.0% | 55.7% | 9.7% | |
| SHALSTAB S1 | 48.0% | 51.2% | 88.6% | |
| SHALSTAB S1 c | 35.7% | 52.5% | 52.7% | |

S1: scenario 1; S2: scenario 2; c: cohesion; (R_{MP}): Model Precision; (R_{MS}): Model sensitivity

Table 7: Summary of unstable areas percent and volume for open land (bare soil) located in the Florencia and Colorado upper basin, for 2 scenarios with the models SHALSTAB and TRIGRS.

| scenario | % of instable area | | | | | |
|-----------------------|--------------------|---------|---------|-------------|---------|---------|
| | Florencia UC | | | Colorado UC | | |
| | SHALSTAB | TRIGRS | | SHALSTAB | TRIGRS | |
| | S1 | S1 | S2 | S1 | S1 | S2 |
| Bare soil Hillslope | 91.0 | 73.6 | 55.3 | 77.9 | 27.2 | 12.9 |
| volume m ³ | 33180.0 | 26970.0 | 13770.0 | 160140.0 | 44010.0 | 15760.0 |

S1: scenario 1; S2: scenario 2; UC: upper catchment;